Article

Phosphatidic acid is an endogenous negative regulator of PIEZO2 channels and mechanical sensitivity

Matthew Gabrielle [1], Yevgen Yudin[1], Yujue Wang[2,3], Xiaoyang Su [2] & Tibor Rohacs [1]✉

Mechanosensitive PIEZO2 ion channels play roles in touch, proprioception, and inflammatory pain. Currently, there are no small molecule inhibitors that selectively inhibit PIEZO2 over PIEZO1. The TMEM120A protein was shown to inhibit PIEZO2 while leaving PIEZO1 unaffected. Here we find that TMEM120A expression elevates cellular levels of phosphatidic acid and lysophosphatidic acid (LPA), aligning with its structural resemblance to lipid-modifying enzymes. Intracellular application of phosphatidic acid or LPA inhibits PIEZO2 but not PIEZO1 activity. Extended extracellular exposure to the non-hydrolyzable phosphatidic acid and LPA analog carbocyclic phosphatidic acid (ccPA) also inhibits PIEZO2. Optogenetic activation of phospholipase D (PLD), a signaling enzyme that generates phosphatidic acid, inhibits PIEZO2 but not PIEZO1. Conversely, inhibiting PLD leads to increased PIEZO2 activity and increased mechanical sensitivity in mice in behavioral experiments. These findings unveil lipid regulators that selectively target PIEZO2 over PIEZO1, and identify the PLD pathway as a regulator of PIEZO2 activity.

PIEZO1 and PIEZO2 are non-selective cation channels activated by mechanical force[1]. PIEZO2 is expressed in peripheral sensory neurons of the dorsal root ganglia (DRG) where it is indispensable for gentle touch and proprioception while also contributing to injury-induced mechanical pain in mice and humans[2]. PIEZO1 has a broader expression profile and is involved in a variety of processes including blood and lymphatic vessel formation, red blood cell volume regulation, and epithelial cell division[3].

Both PIEZO1 and PIEZO2 channels are inhibited by non-specific blockers of mechanically activated ion channels such as gadolinium, ruthenium red, and GsMTx4[4]. Screening small molecule libraries resulted in the discovery of selective activators of PIEZO1 channels (Yoda1, Jedi1, and Jedi2)[5,6], but the same screens did not identify chemical activators of PIEZO2. Chemical modification of Yoda1 resulted in Dooku[7], a compound that antagonizes Yoda1 activation of PIEZO1. Currently, there are no known endogenous or exogenous inhibitors that selectively inhibit PIEZO2 over PIEZO1. Selective PIEZO2 inhibitors would be highly valuable research tools and would have substantial therapeutic potential against mechanical pain[2,4].

We have recently shown that co-expression of the TMEM120A (a.k.a. TACAN) protein robustly inhibited PIEZO2, but not PIEZO1 channel activity[8]. TMEM120A was proposed earlier to be an ion channel involved in sensing mechanical pain[9], but subsequent studies raised doubts about its ability to function as an ion channel and respond to mechanical stimuli[8,10-13]. Structural studies revealed that TMEM120A is a homodimer of two subunits with six transmembrane segments in each[10,12,13] with structural homology to a lipid-modifying enzyme, elongation of very long-chain fatty acids 7 (ELOVL7)[14], that elongates the acyl-chains of lipid-coenzyme A (CoA) species[15]. Consistent with its potential function as a lipid-modifying enzyme, the TMEM120A structures contained a CoA molecule[10,12,13]. The specific enzymatic activity of TMEM120A, however, is unknown[10], see our recent review for details[16].

[1]Department of Pharmacology, Physiology & Neuroscience, Rutgers University New Jersey Medical School, Newark, NJ, USA. [2]Metabolomics Shared Resource, Rutgers Cancer Institute of New Jersey, New Brunswick, NJ, USA. [3]Present address: School of Pharmaceutical Sciences, Tsinghua—Peking Center for Life Sciences, Beijing Frontier Research Center for Biological Structure, Tsinghua University, Beijing, China. ✉e-mail: rohacsti@njms.rutgers.edu

Here, we hypothesized that TMEM120A inhibited PIEZO2 currents by altering cellular lipid content and aimed to identify the lipid regulator that selectively inhibits PIEZO2 without affecting PIEZO1 activity. To achieve this, we conducted liquid chromatography-tandem mass spectrometry (LC-MS/MS) experiments, which revealed that TMEM120A expression robustly elevates phosphatidic acid and lysophosphatidic acid (LPA) levels with saturated acyl chains. Furthermore, we observed that mutating a putative catalytic residue in TMEM120A reduced its inhibitory effect. Intracellular delivery of phosphatidic acid or LPA through the whole-cell patch pipette inhibited PIEZO2 activity while leaving PIEZO1 unaffected. Long-term incubation with carbocyclic phosphatidic acid (ccPA), a metabolically inert analog of phosphatidic acid and LPA, effectively inhibited heterologously expressed PIEZO2 channels, and decreased both the proportion and amplitudes of rapidly adapting mechanically activated currents in DRG neurons. Optogenetic activation of phospholipase D (PLD), a signaling enzyme that generates phosphatidic acid, inhibited PIEZO2, but not PIEZO1 channel activity. Inhibition of PLD enzymes potentiated both heterologously expressed and native PIEZO2, while not affecting PIEZO1 activity. PLD inhibition also increased mechanical sensitivity in mice in behavioral experiments. We identify phosphatidic acid and LPA as specific inhibitors of PIEZO2 channels, and our data indicate that PLD enzymes, which produce phosphatidic acid, modulate PIEZO2 activity. These findings unveil lipid regulators that selectively target PIEZO2 over PIEZO1, and hold promise for the development of specific PIEZO2 inhibitors.

Results

Changes in cellular lipid content mediate inhibition of PIEZO2 by TMEM120A

Earlier research indicates that expression of TMEM120A results in robust inhibition of PIEZO2, but not PIEZO1 channels[8]. TMEM120A shows structural homology to the long-chain fatty acid elongase enzyme ELOVL7[10,12,13], but its potential lipid-modifying enzymatic activity has not yet been determined[16]. To test the hypothesis that TMEM120A inhibits PIEZO2 activity by modifying cellular lipid content, we performed LC-MS/MS experiments in cells transfected with TMEM120A and compared them to mock (vector) transfected cells, and cells transfected with TMEM120B (a homolog of TMEM120A that did not inhibit PIEZO2 activity[8]). We used Neuro2A (N2A) cells in which endogenous PIEZO1 was deleted using CRISPR (N2A-Pz1-KO)[17,18]. We found this cell line to be a good model system to study heterologously expressed PIEZO2 channels[8], and also used it for most electrophysiology experiments in this study. Cells transfected with TMEM120A showed a large, 4-fold increase in the levels of phosphatidic acid and lysophosphatidic acid (LPA) with fully saturated acyl chains (Fig. 1a). Diacylglycerol (DAG) showed a small, ~20% increase, and triacylglycerol (TG), showed a 1.9-fold increase compared to control, mock-transfected cells (Fig. 1a). Considering that transfection efficiency in these experiments was approximately 40%, these bulk changes likely underestimate the changes at the individual cell level.

Cells transfected with TMEM120B did not show these changes, except for a small, ~30% increase in TG levels (Fig. 1a). These lipids are intermediates in the Kennedy pathway of TG synthesis from glycerol-3 phosphate (Fig. 1b), and the changes were largely restricted to lipid species with fully saturated acyl chains. We observed either no, or smaller changes in monounsaturated and polyunsaturated LPA, phosphatidic acid, DAG, and TG (Supplementary Fig. 1). Furthermore, we did not observe significant changes in the level of various other lipids in any degree of saturation including but not limited to ceramide, sphingomyelin, phosphatidylglycerol, phosphatidylserine or phosphatidylinositol (Supplementary Table 1).

Next, we mutated a putative catalytic residue that interacts with CoA in the TMEM120A structures (Fig. 1c), and we found that co-expressing this TMEM120A-W193A mutant induced a significantly

smaller inhibition of PIEZO2 than the wild-type TMEM120A (Fig. 1d–h). We obtained similar results with a triple mutant of TMEM120A, in which we introduced two additional mutations in two adjacent histidine residues that were implicated in the catalytic activity of ELOVL[10] (W193A-H196A-H197A; AxxAA) (Supplementary Fig. 2a–d).

In these experiments, we used TMEM120A, and its mutants tagged with the red fluorescent protein tdTomato, and PIEZO2 tagged with EGFP. Supplementary Fig. 2e–g shows that tdTomato fluorescence in total internal reflection fluorescence (TIRF) experiments was not different in cells transfected with wild-type or W193A or AxxAA mutants of TMEM120A. TIRF microscopy shows fluorescence in the plasma membrane and a narrow sub-plasmalemmal region, thus these experiments indicate that the reduced inhibition by the mutant TMEM120A was not caused by reduced surface expression. EGFP fluorescence in the TIRF mode was also not different between cells transfected with PIEZO2-GFP and the mutant and wild-type TMEM120A or tdTomato, indicating that inhibition of PIEZO2 by TMEM120A was not caused by reduced surface expression, a finding consistent with our earlier result[8].

With no change in surface expression, we tested how these mutations affect TMEM120A-induced formation of LPA and phosphatidic acid. We utilized an enzyme-based assay[19] to quantify the total LPA/phosphatidic acid content of N2A-Pz1-KO cells expressing these mutant constructs (Supplementary Fig. 2h). Both the W193A and AxxAA mutants produced total LPA/phosphatidic acid levels that were still modestly elevated but not significantly greater than mock-transfected cells (Supplementary Fig. 2h). Together these data indicate that residues interacting with the putative CoA substrate are important for TMEM120A's capacity for increasing the levels of LPA/phosphatidic acid and inhibiting PIEZO2.

We also found that inhibiting glycerol-3-phosphate acyltransferase (GPAT) by using 100 μM FSG67, the first enzyme in the Kennedy pathway (Supplementary Fig. 3a), significantly reduced the inhibition of PIEZO2 currents by TMEM120A (Supplementary Fig. 3b–f). The reduction of inhibition was small, which is likely due to an alternative pathway to generate LPA from glycerol-3-phosphate by the DHAPAT and Acyl-DHAP Reductase enzymes (Supplementary Fig. 3a). Overall, these data indicate that the changes in lipid composition induced by TMEM120A play a role in the inhibition of PIEZO2.

Phosphatidic acid and LPA inhibit PIEZO2 but not PIEZO1 channels

To identify the lipid molecule(s) that inhibit PIEZO2 activity, we performed whole-cell patch clamp experiments in N2A-Pz1-KO cells transfected with PIEZO2, or PIEZO1, and evoked mechanically activated inward currents using increasing indentations with a blunt glass probe (Fig. 2). Consistent with earlier results[17,20,21] non-transfected N2A-Pz1-KO cells did not display mechanically activated currents in response to indentations with the blunt glass probe (Supplementary Fig. 3g), but cells expressing PIEZO2 (Fig. 2a–d) or PIEZO1 (Fig. 2e–h) showed characteristic rapidly inactivating mechanically activated currents. We delivered various lipids to the intracellular compartment through the whole-cell patch pipette, and compared mechanically activated currents to those in cells with lipid-free pipette solution.

First, we tested the effect of phosphatidic acid which showed the most robust increase in TMEM120A transfected cells (Fig. 1a). Mechanically activated PIEZO2 currents were robustly inhibited in experiments where we included the water-soluble short acyl-chain dioctanoyl phosphatidic acid (300 μM) in the whole-cell patch pipette, compared to control cells (Fig. 2a–d). In these experiments, we increased the stimulation depth in each cell until the seal was lost, but only plotted currents up to 8 μm in Fig. 2a for visual clarity. In the control group, 100% of cells displayed mechanically activated currents while in the phosphatidic acid group, only 42.9% of the cells responded. The mechanical threshold to evoke currents was significantly
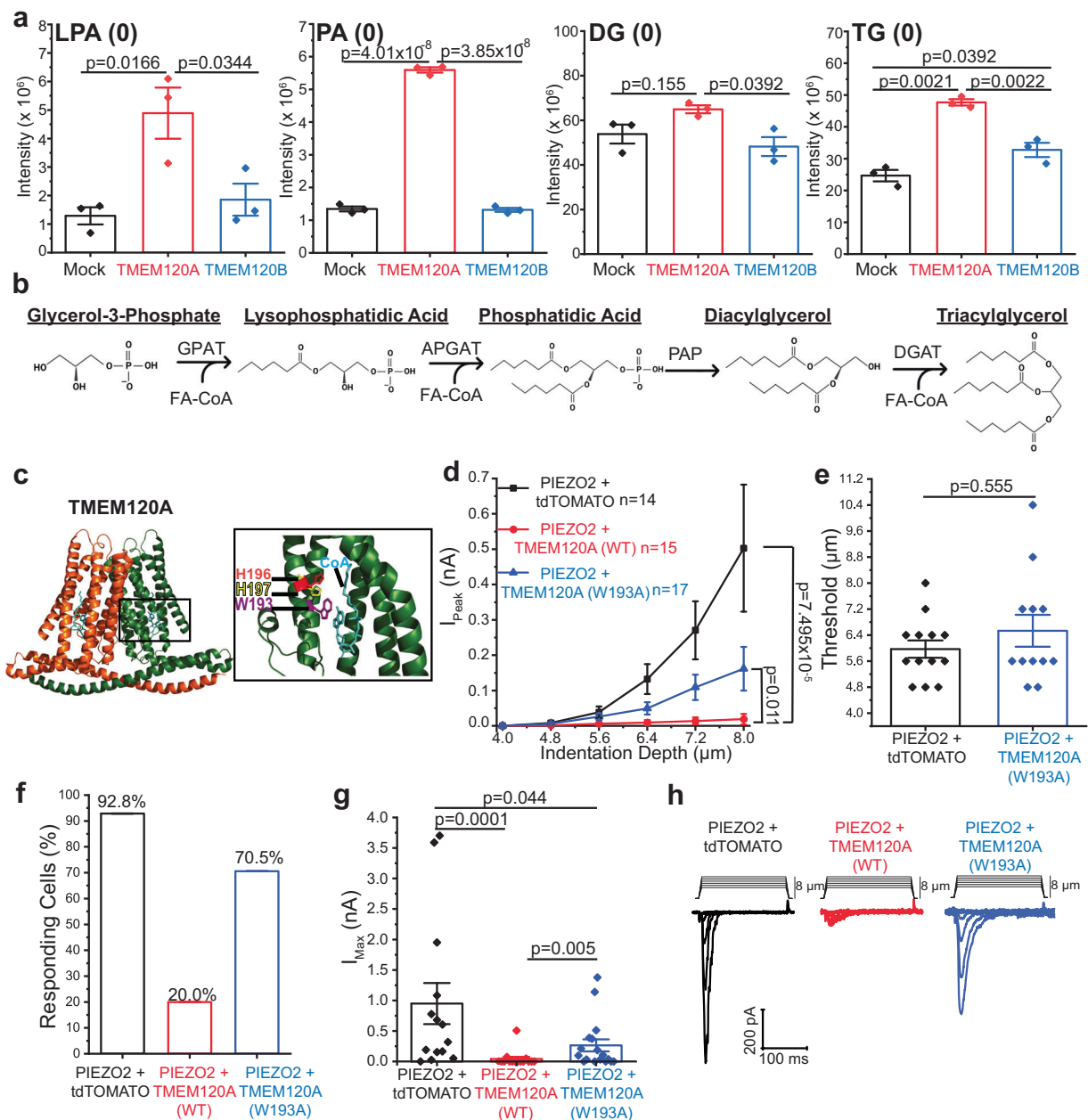
Fig. 1 | Changes in cellular lipid content mediate inhibition of PIEZO2 by TMEM120A. a LC-MS/MS experiments using N2A-Pz1-KO cells transiently transfected with vector (mock, black), TMEM120A (red), or TMEM120B (blue) as described in the methods section. Scatter plots and mean ± SEM of the relative saturated lipid intensities detected for $n = 3$ independent transfections for LPA (ANOVA, $F_{(2,6)} = 9.274$, $p = 0.0146$), phosphatidic acid (PA) (ANOVA, $F_{(2,6)} = 1148$, $p = 1.77 \times 10^{-8}$), DG (ANOVA, $F_{(2,6)} = 5.528$, $p = 0.0435$), TG (ANOVA, $F_{(2,6)} = 44.500$, $p = 0.0002$). Post-hoc Tukey test p-values are displayed on the plots. **b** Scheme of the Kennedy pathway for de novo TG synthesis. Lipids are depicted with short acyl chains because of spatial restrictions. **c** Structure of TMEM120A with magnified (black box) residues interacting with CoA generated using PyMOL from the publicly available pdb file 7F3T[12]. **d–h** Whole-cell voltage-clamp experiments at −60 mV in N2A-Pz1-KO cells transiently transfected with PIEZO2-GFP, and tdTOMATO (black,

$n = 14$ cells), TMEM120A-tdTom-WT (red, $n = 15$ cells), or TMEM120A-tdTom-W193A (blue, $n = 17$ cells). **d** Mechanically activated currents were evoked by indentations of increasing depth with a blunt glass probe. Current amplitudes are plotted (mean ± SEM) and statistical differences for the area under the curve (AUC) for 4.0–8.0 μm stimuli are calculated with the two-tailed Mann–Whitney test. **e** Scatter and mean ± SEM for the threshold of membrane indentation to elicit mechanically activated current (two-tailed Mann–Whitney). Mechanical threshold is only quantifiable for cells where membrane indentation elicited current, thus non-responding cells reduce the n for PIEZO2-GFP + tdTOMATO to $n = 13$ cells and for PIEZO2-GFP + TMEM120A-tdTom-W193a to $n = 12$ cells. **f** Percentage of responding cells. **g** Scatter and mean ± SEM for maximum currents (Kruskal–Wallis, $\chi^2 = 17.467$, df = 2, $p = 0.0001$; two-tailed Mann–Whitney tests displayed). **h** Representative current traces.

lower in control cells than in cells with the intracellular phosphatidic acid application (Fig. 2b), and the maximal current, evoked by the largest stimulus before seal rupture, was also significantly higher in control cells compared to phosphatidic acid-treated cells (Fig. 2c). As shown in Fig. 2e–h, PIEZO1 currents were not affected by dioctanoyl phosphatidic acid. Both mechanical threshold (Fig. 2f), and maximal

PIEZO1 currents (Fig. 2g) were similar in control and in phosphatidic acid-treated cells. The lack of inhibition by phosphatidic acid is consistent with PIEZO1 channels also not being inhibited by TMEM120A[8]. The inactivation time constant (tau) was not different between control and phosphatidic acid-treated cells for PIEZO2 (Supplementary Fig. 4a) and PIEZO1 (Supplementary Fig. 4b).
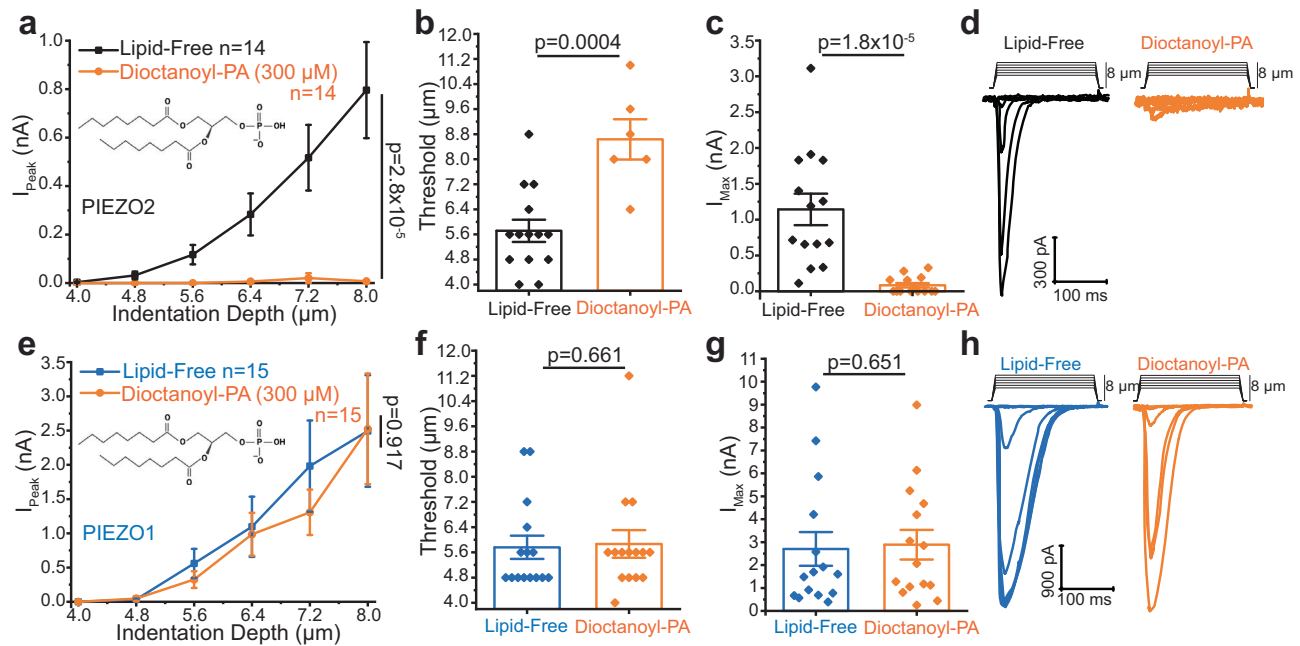
Fig. 2 | Phosphatidic acid inhibits PIEZO2 but not PIEZO1. Whole-cell patch-clamp experiments at −60 mV in N2A-Pz1-KO cells transiently transfected with PIEZO2-GFP or PIEZO1-GFP with patch-pipette solution supplemented with the indicated lipids as described in the methods section. **a**–**d** PIEZO2-GFP transfected cells supplemented with 300 µM dioctanoyl-phosphatidic acid (PA, $n = 14$ cells) or lipid-free ($n = 15$ cells). **a** Current amplitudes are plotted (mean ± SEM) and statistical difference for the area under curve (AUC) for 4.0–8.0 µm stimuli calculated with the two-tailed Mann–Whitney test. **b** Membrane indentation depth threshold to elicit mechanically activated current (two-tailed t-test). Mechanical threshold is only quantifiable for cells where membrane indentation elicited current, thus non-responding cells reduce the n for dioctanoyl-PA treated cells to $n = 6$ cells. **c** Maximum current amplitudes (Mann–Whitney). **d** Representative current traces. **e**–**h** PIEZO1-GFP-transfected cells supplemented with 300 µM dioctanoyl-PA ($n = 15$ cells) or lipid-free ($n = 15$ cells). **e** Current amplitudes are plotted (mean ± SEM) and the statistical difference of AUC for 4.0–8.0 µm stimuli is calculated with the two-tailed Mann–Whitney test. **f** Membrane indentation depth threshold to elicit mechanically activated current (two-tailed Mann–Whitney). **g** Maximum current amplitudes (two-tailed Mann–Whitney). **h** Representative current traces. All bar graphs are plotted with scatter and mean ± SEM.

To determine whether the presence of phosphatidic acid intracellularly was necessary to affect PIEZO2 channels, we also applied the lipid extracellularly (Supplementary Fig. 5). N2A-Pz1-KO cells expressing PIEZO2 were stimulated with a fixed membrane-indentation depth that produced sub-maximal currents every 30 s. Dioctanoyl phosphatidic acid (300 µM) was perfused for 8 min to mimic the time course of experiments where the patch pipette solution was supplemented with the lipid (5 min of incubation once seal was formed for dialysis + 3 min recording time). We did not observe any significant changes in PIEZO2 currents when perfused with dioctanoyl phosphatidic acid (Supplementary Fig. 5d, e) indicating that phosphatidic acid's intracellular localization is necessary to inhibit PIEZO2.

Next, we tested the effect of LPA, a lipid that also showed a significant increase in TMEM120A-expressing cells (Fig. 1a). Inclusion of palmitoyl LPA (30 µM) in the patch pipette also inhibited PIEZO2 channels (Fig. 3a–d). The area under the curve between 4 and 8 µm indentations was significantly lower in LPA-treated cells (Fig. 3a), and the mechanical threshold to evoke currents was significantly lower in control cells than in cells with intracellular palmitoyl LPA application (Fig. 3b). The maximal current evoked was not significantly higher in control cells compared to palmitoyl LPA-treated cells ($p = 0.08$) (Fig. 3c). Intracellular application of palmitoyl LPA did not inhibit mechanically activated PIEZO1 currents (Fig. 3e–h). Neither the threshold for mechanically activated currents (Fig. 3f), nor the maximal PIEZO1 current (Fig. 3g) were different between control and LPA-treated cells. The inactivation time constant (tau) was not different between cells treated with palmitoyl LPA for either PIEZO2 (Supplementary Fig. 4c) or PIEZO1 (Supplementary Fig. 4d).

We also tested whether LPA with a slightly longer acyl-chain and increasing degrees of unsaturation would also affect PIEZO2 activity. To achieve this, we supplemented the patch-pipette solution with

30 µM stearoyl LPA (C18:0), or 30 µM oleoyl LPA (C18:1) or 30 µM linoleoyl LPA (C18:2), (Fig. 3i–l). The area under the curve between 4 and 8 µm indentations was significantly lower in cells treated with all three of these lipids (Fig. 3i). The mechanical threshold was only significantly increased in cells treated with the fully saturated stearoyl LPA (Fig. 3j), but all three of these LPA species reduced the maximal evoked PIEZO2 currents (Fig. 3k). We did not observe any differences in tau values for PIEZO2 when treated with stearoyl, oleoyl or linoleoyl LPA (Supplementary Fig. 4e).

While we did not detect significant changes to the levels in other phospholipids (Supplementary Table 1), we tested whether other negatively charged phospholipids may also affect PIEZO2 channels (Supplementary Fig. 6a–h). First, we supplemented the patch-pipette solution with dioctanoyl phosphatidylglycerol (PG; 300 µM), which did not yield any significant changes in PIEZO2 currents or mechanical threshold (Supplementary Fig. 6a–d). We also observed no significant changes when we supplemented PIEZO2-expressing cells with dioctanoyl phosphatidylserine (PS; 300 µM) (Supplementary Fig. 6e–h). Dioctanoyl PG did not affect the inactivation kinetics of PIEZO2 (Supplementary Fig. 4f). Dioctanoyl PS did modestly but significantly reduced PIEZO2's average inactivation time constant (Supplementary Fig. 4g). These data suggest that the free inorganic phosphate headgroup of phosphatidic acid is important for its effect on PIEZO2 activity.

Intriguingly, the lipids that showed the largest increase in TMEM120A transfected cells, were generated by enzymes that require acyl-CoA (Fig. 1a). TMEM120A shares substantial structural homology with an acyl-CoA elongase (ELOVL7)[10,13,22], and TMEM120A has been reported to increase CoA levels in cancer cells[23]. This may suggest that TMEM120A provides acyl-CoA to these enzymatic steps. Long-acyl-chain CoA is known to modulate ion channels[24,25] therefore we tested if including palmitoyl CoA (30 µM) in the whole-cell patch pipette affects
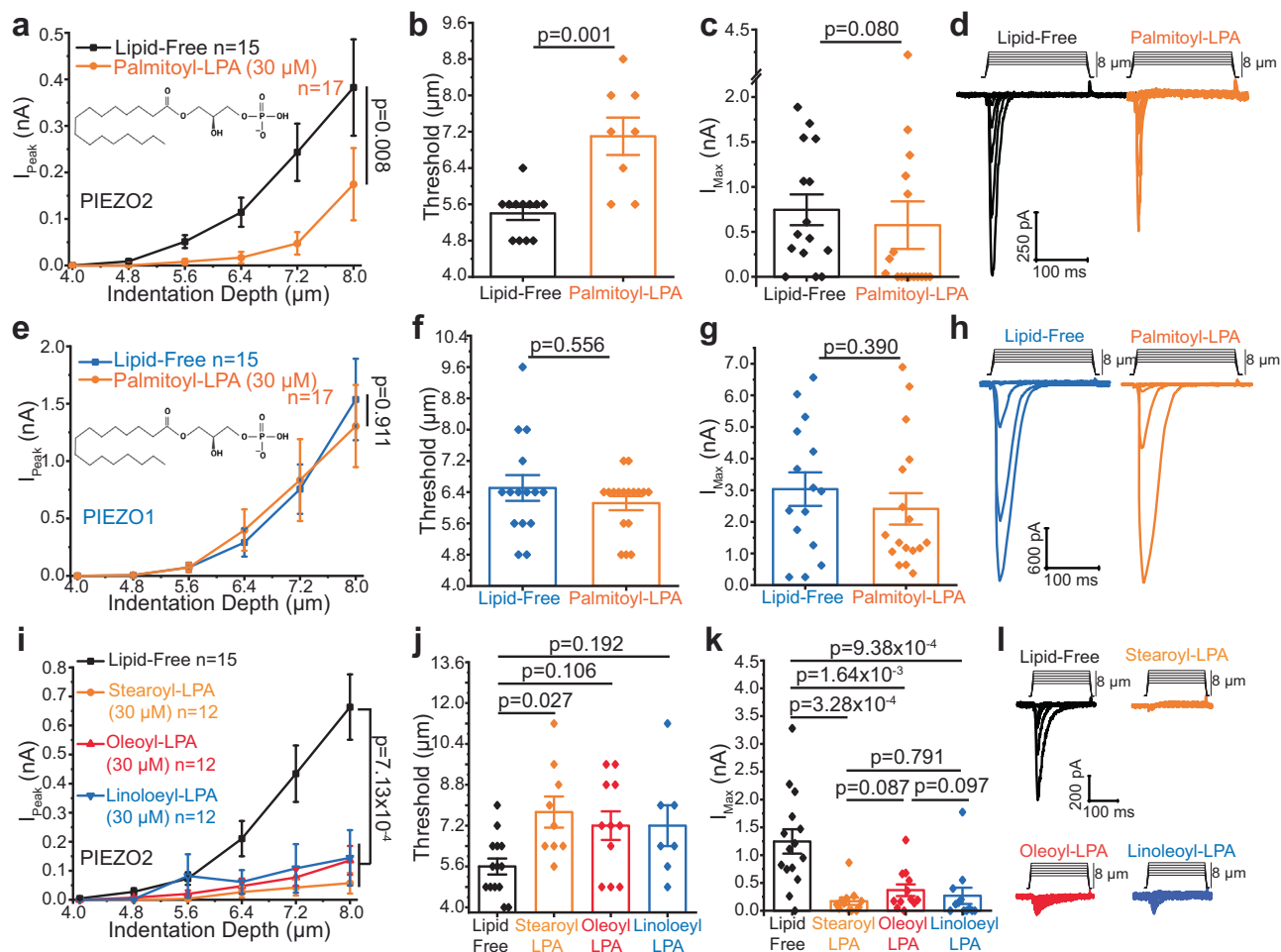
Fig. 3 | LPA inhibits PIEZO2 but not PIEZO1. Whole-cell patch-clamp experiments at −60 mV in N2A-Pz1-KO cells transiently transfected with PIEZO2-GFP or PIEZO1-GFP with patch-pipette solution supplemented with the indicated lipids as described in the methods section. **a**−**d** PIEZO2-GFP-expressing cells supplemented with 30 μM palmitoyl-LPA ($n = 17$ cells) or lipid-free ($n = 15$ cells). **a** Current amplitudes are plotted (mean ± SEM) and statistical difference of AUC for 4.0−8.0 μm stimuli calculated with the two-tailed Mann−Whitney test. **b** Membrane indentation depth threshold to elicit mechanically activated currents (two-tailed Mann−Whitney). Mechanical threshold is only quantifiable for cells where membrane indentation elicited current, thus non-responding cells reduce the n for lipid-free treated cells to $n = 12$ cells and for palmitoyl-LPA-treated cells to $n = 8$ cells. **c** Maximum current amplitudes (two-tailed Mann−Whitney). **d** Representative current traces. **e**−**h** PIEZO1-GFP expressing cells supplemented with 30 μM palmitoyl-LPA ($n = 17$ cells) or lipid-free ($n = 15$ cells). **e** Current amplitudes are plotted (mean ± SEM) and the statistical difference of AUC for 4.0−8.0 μm stimuli is calculated with the two-tailed Mann−Whitney test. **f** Membrane indentation depth threshold to elicit mechanically activated current (two-tailed Mann−Whitney). **g** Maximum current amplitudes (two-tailed Mann−Whitney). **h** Representative

current traces. **i**−**l** PIEZO2-GFP expressing cells supplemented with 30 μM stearoyl-LPA ($n = 12$ cells), 30 μM oleoyl-LPA ($n = 12$ cells), 30 μM linoleoyl-LPA ($n = 12$ cells), or lipid-free ($n = 15$ cells). **i** Current amplitudes are plotted (mean ± SEM). Statistical comparison of AUC for 4.0−8.0 μm stimuli calculated with the Kruskal−Wallis test (p-value displayed on plot; $\chi^2 = 16.979$, df = 3, $p = 7.13 \times 10^{-4}$). Post-hoc two-tailed Mann−Whitney tests: Lipid-Free/Stearoyl-LPA, $p = 3.28 \times 10^{-4}$; Lipid-Free/Oleoyl-LPA, $p = 1.64 \times 10^{-3}$; Lipid-Free/Linoleoyl-LPA, $p = 9.28 \times 10^{-4}$; Stearoyl-LPA/Oleoyl-LPA, $p = 0.087$; Stearoyl-LPA/Linoleoyl-LPA, $p = 0.791$; Oleoyl-LPA/Linoleoyl-LPA, $p = 0.0972$. **j** Membrane indentation depth threshold to elicit mechanically activated current (ANOVA, $F(3,37) = 3.58$, $p = 0.022$; post-hoc Tukey tests displayed). Mechanical threshold is only quantifiable for cells where membrane indentation elicited current, thus non-responding cells reduce the n for lipid-free treated cells to $n = 14$ cells, for stearoyl-LPA-treated cells to $n = 9$ cells, for oleoyl-LPA-treated cells to $n = 11$ cells, and for linoleoyl-LPA-treated cells to $n = 7$ cells. **k** Maximum current amplitudes (Kruskal−Wallis, $\chi^2 = 20.374$, df = 3, $p = 1.42 \times 10^{-4}$; post-hoc two-tailed Mann−Whitney tests displayed). **l** Representative current traces. All bar graphs are plotted with scatter and mean ± SEM.

PIEZO2 activity. Supplementary Fig. 6i−l. shows that amplitudes of mechanically induced currents in PIEZO2-expressing cells were similar to those in cells that were dialyzed with palmitoyl-CoA and control cells. The inactivation time constant (tau) for PIEZO2 currents was also not different between control and palmitoyl-CoA treated cells (Supplementary Fig. 4h). These data show that acyl-CoA is unlikely to be the lipid responsible for PIEZO2 inhibition upon TMEM120A expression.

A non-metabolizable analog of phosphatidic acid and LPA inhibits PIEZO2 channels

Our experiments so far showed that phosphatidic acid and LPA inhibit PIEZO2 currents when delivered intracellularly. Phosphatidic acid and

LPA are both charged, thus unlikely to rapidly cross the plasma membrane, and also metabolically unstable, and can be converted to other lipids inside and outside the cell. LPA also activates cell surface receptors, which would complicate the interpretation of results with extracellular application. Carbocyclic Phosphatidic Acid (ccPA), is a metabolically stable analog of phosphatidic acid and LPA that does not activate LPA receptors[26]. It was also reported that ccPA administration reduced mechanical allodynia in rats but whether ccPA affects PIEZO2 channel activity has not been tested[27]. To explore the possibility that the extracellular application of this phosphatidic acid and LPA analog can be used to modulate PIEZO2 activity, we tested the effect of long-term (24−32 h) incubation with ccPA on mechanically activated PIEZO2

currents. We incubated N2A-Pz1-KO cells expressing PIEZO2 with 300 μM ccPA, and we found that mechanically activated currents were inhibited compared to control cells (Fig. 4a–d). Both maximal currents (Fig. 4c) and the area under the curve between 4 and 8 μm stimulations (Fig. 4a) were significantly lower in ccPA-treated cells, but the threshold to elicit mechanically induced currents was not different (Fig. 4b).

Next, we tested if endogenous rapidly adapting mechanically activated currents in DRG neurons are inhibited by ccPA. Figure 4e shows that the proportion of neurons displaying rapidly adapting MA currents decreased from 65% to 25 % when the cells were treated overnight with ccPA. We normalized the current amplitudes of DRG neurons to each cell's capacitance (current density; pA/pF) given the heterogeneity of cell size and expression patterns within the population. In the neurons that displayed rapidly adapting mechanically activated currents, the maximal current density was significantly lower in cells treated with ccPA (Fig. 4g). There was a compensatory increase in the proportion of non-responding cells in the ccPA-treated group. The proportion of slowly adapting and intermediate currents also increased (Fig. 4e), but their amplitudes were not different in ccPA-treated and control cells (Fig. 4h, i). The mechanical threshold of rapidly adapting mechanically activated currents did not change in ccPA-treated cells (Fig. 4j), but the mechanical threshold of intermediate and slowly adapting currents significantly decreased (Fig. 4k, l). Since ccPA, PA and LPA treatment did not change the inactivation time constant of expressed recombinant PIEZO2 currents (Supplementary Fig. 4a, c, e, i), the increase in the proportion of intermediate and slowly adapting current is likely due to unmasking of slowly adapting and intermediate currents by PIEZO2 inhibition, and potentially a compensatory increase in those currents. Overall, these data indicate that ccPA treatment inhibits both recombinant and endogenous PIEZO2-mediated mechanically activated currents.

Phospholipase D (PLD) regulates PIEZO2 but not PIEZO1 channels

Phosphatidic acid can also be generated by phospholipase D enzymes from phosphatidylcholine[28]. To test if PLD activation modulates PIEZO2 activity, we used the opto-PLD system, where PLD activity in the plasma membrane can be induced by blue light[29]. This system is based on the recruitment of a PLD enzyme fused to the cryptochrome 2 (CRY2) plant protein which undergoes heterodimerization with the truncated cryptochrome-interacting basic-helix-loop-helix 1, aa1-170 (CIBN) in response to blue light. CIBN is targeted to the plasma membrane, and therefore blue light induces a translocation of PLD to the plasma membrane (Fig. 5a). We found that PIEZO2 activity is inhibited by blue light exposure in cells expressing the two components of the opto-PLD system (Fig. 5b, c, e). When the components of the Opto-PLD system containing a catalytically inactive PLD mutant (H170A) were co-transfected, blue light illumination did not inhibit PIEZO2 (Fig. 5b–d). Mechanically activated PIEZO1 currents were not inhibited by activating the opto-PLD system with blue light (Supplementary Fig. 7).

Our data so far show that acutely activating PLD inhibits PIEZO2 activity. Next, we tested if endogenous basal PLD activity contributes to the regulation of PIEZO2 channels. To achieve this, we treated PIEZO2-expressing N2A-Pz1-KO cells with the broad spectrum PLD inhibitor FIPI (500 nM). As shown in Fig. 6b–e, mechanically activated PIEZO2 currents were significantly increased by FIPI treatment. The mechanical threshold to evoke PIEZO2 currents was significantly lower in FIPI-treated cells (Fig. 6c) and the maximal current amplitude was significantly higher (Fig. 6d).

PIEZO1 currents, on the other hand, were not potentiated by FIPI (Fig. 6f–i), which is consistent with our finding that PIEZO1 currents were not affected by phosphatidic acid (Fig. 2e). The inactivation time

constant (tau) was similar in FIPI-treated and control cells for both PIEZO2 and PIEZO1 currents (Supplementary Fig. 8a, b).

There are two mammalian PLD enzymes, PLD1 and PLD2. To test which isoform is responsible for the basal regulation of PIEZO2 activity, we co-expressed PLD1 or PLD2 with PIEZO2 in N2A-Pz1-KO cells. Figure 6j–m shows that co-expression of PLD2, but not PLD1 significantly inhibited PIEZO2 activity. The maximal currents in PLD2 expressing cells were significantly lower than in control cells (Fig. 6l). Mechanical threshold in PLD2 expressing cells was not significantly higher ($p = 0.07$) (Fig. 6k). The inactivation time constant (tau) was similar in cells expressing PLD1 or PLD2 and in control cells (Supplementary Fig. 8c). The inhibition of PIEZO2 currents by overexpressing PLD2 but not by PLD1 is consistent with PLD2, but not PLD1 showing constitutive activity[30].

PLD modulates native rapidly adapting mechanically activated currents in peripheral sensory neurons and mechanical sensitivity in mice

Our data with recombinant PIEZO2 currents show that these channels can be modulated by the PLD pathway. Next, we tested if endogenous PLD activity also regulates PIEZO2 channels in their native environment. First, we performed experiments in human induced pluripotent stem cell (hiPSC)-derived sensory neurons (Anatomic Incorporated)[31]. Consistent with earlier results[31], these cells displayed predominantly rapidly adapting mechanically activated currents. Similarly to isolated mouse DRG neurons, we normalized the hiPSC-derived sensory neurons' current amplitudes to each cell's capacitance (current density; pA/pF) as these neurons continue to mature and change expression levels over time. As shown in Fig. 7a, mechanically activated current densities were significantly higher in FIPI-treated cells, compared to control cells. Mechanical thresholds were significantly lower (Fig. 7b), and maximal current densities were significantly higher (Fig. 7c) in FIPI-treated cells compared to control cells.

Next, we tested the effect of the PLD inhibitor FIPI in DRG neurons displaying rapidly adapting mechanically activated currents. We first performed whole-cell voltage-clamp experiments to identify neurons that display rapidly adapting mechanically activated currents, using the same increasing indentation depth protocol we used in our experiments so far, but we stopped mechanical stimulation shortly after clear rapidly adapting currents appeared, to avoid losing the seal. The mechanical threshold to elicit rapidly adapting currents was significantly lower in FIPI-treated cells compared to control cells (Fig. 7e). Then on the same neurons, we performed current-clamp measurements to test the mechanical threshold to elicit action potentials. As shown in Fig. 7f, the indentation depth threshold to elicit action potentials was significantly lower in FIPI-treated cells, than in control neurons. We also tested the current injection threshold to elicit action potentials. As shown in Fig. 7g, the current injection thresholds to elicit action potentials were similar in FIPI-treated and control cells. The resting membrane potential was also not significantly different between control (of -50.4 ± 0.84 mV) and FIPI-treated neurons (-48.2 ± 1.56, $p = 0.252$) (Supplementary Fig. 9c). These data indicate that the effect of FIPI on the mechanical threshold was not due to the increased general excitability of DRG neurons.

To test if PLD inhibition by FIPI can modulate PIEZO2-mediated touch sensation, we injected mice with FIPI intraperitoneally, and tested their mechanical sensitivity using von Frey filaments (Fig. 7h). We found that mice injected with FIPI had significantly lower 50% mechanical threshold to withdraw their hind paw from von Frey filaments (Fig. 7i). This is consistent with FIPI potentiating PIEZO2 currents and lowering firing threshold evoked by mechanical stimuli in DRG neurons. Paw withdrawal latencies to thermal stimuli on the other hand were not significantly different in FIPI-injected and control mice (Fig. 7j) indicating that the effect of FIPI was specific to mechanical stimuli.
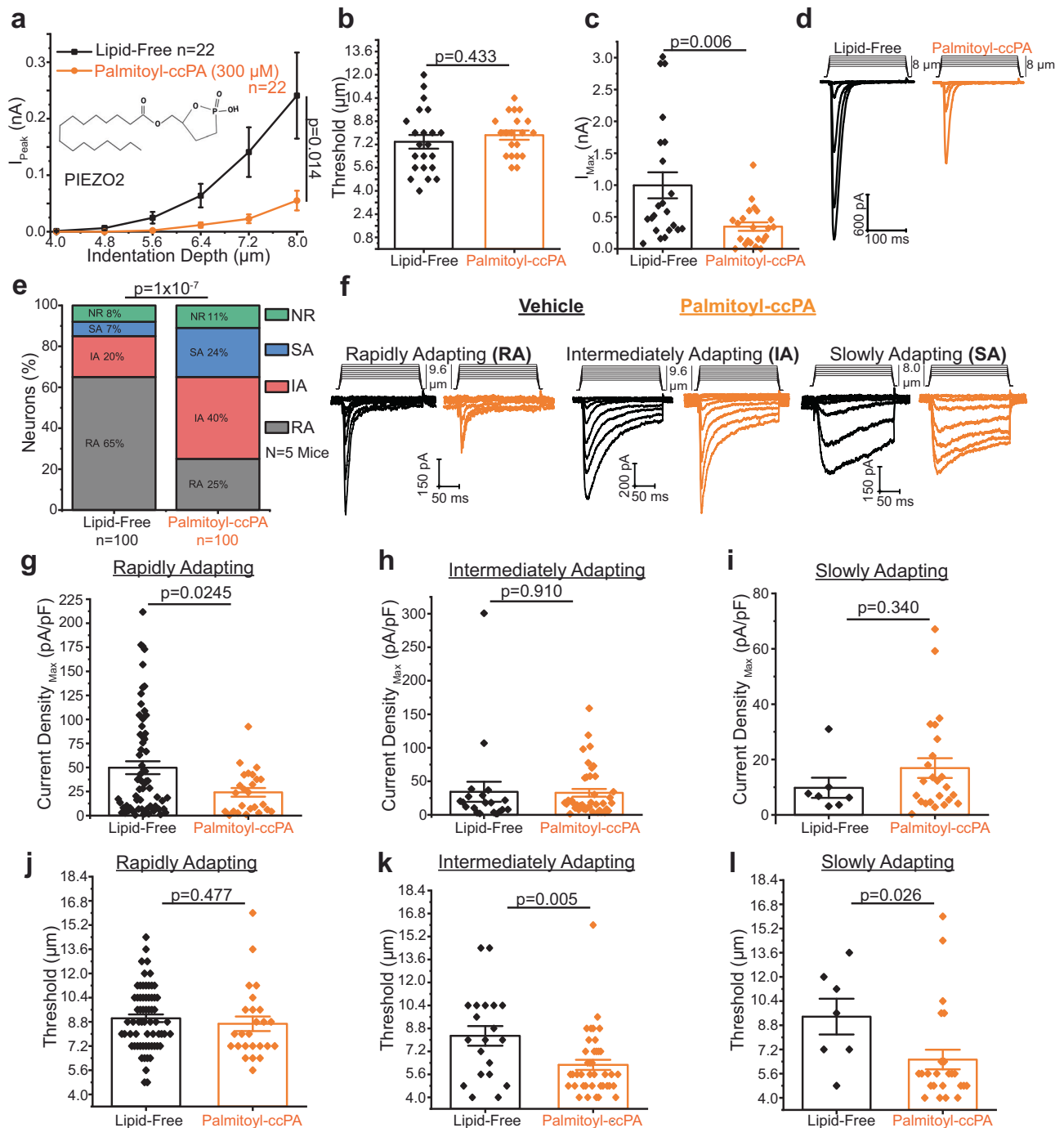
Fig. 4 | Extracellular application of ccPA inhibits PIEZO2 currents. Whole-cell patch-clamp experiments were performed at −60 mV as described in the methods section. **a**−**d** N2A-Pz1-KO cells transiently transfected with PIEZO2-GFP mock-treated (black, $n = 24$ cells) or treated with extracellular palmitoyl-ccPA overnight (orange, $n = 24$ cells). **a** Current amplitudes are plotted (mean ± SEM) and statistical difference in the area under the curve (AUC) for 4.0–8.0 μm stimuli is calculated with the two-tailed Mann–Whitney test. **b** Membrane indentation depth threshold to elicit mechanically activated currents (two-tailed t-test). Mechanical threshold is only quantifiable for cells where membrane indentation elicited current, thus non-responding cells reduce the n for palmitoyl-ccPA-treated cells to $n = 20$ cells. **c** Maximum current amplitudes (two-tailed Mann–Whitney). **d** Representative current traces. **e**−**l** Isolated mouse DRG neurons mock-treated (black, $n = 100$ cells)

or treated with extracellular palmitoyl-ccPA overnight (orange, $n = 100$ cells). **e** Proportion of rapidly adapting (RA), intermediately adapting (IA), slowly adapting (SA), and non-responders (NR). Chi-squared test. **f** Representative current traces. **g** Rapidly adapting maximum current density (two-tailed t-test). **h** Intermediate adapting maximum current density (two-tailed t-test). **i** Slowly adapting maximum current density (two-tailed Mann–Whitney). **j** Membrane indentation depth threshold to elicit rapidly adapting current (two-tailed t-test). **k** Membrane indentation depth threshold to elicit intermediately adapting current (two-tailed t-test). **l** Membrane indentation depth threshold to elicit slowly adapting current (two-tailed Mann–Whitney). All bar graphs are plotted with scatter and mean ± SEM.
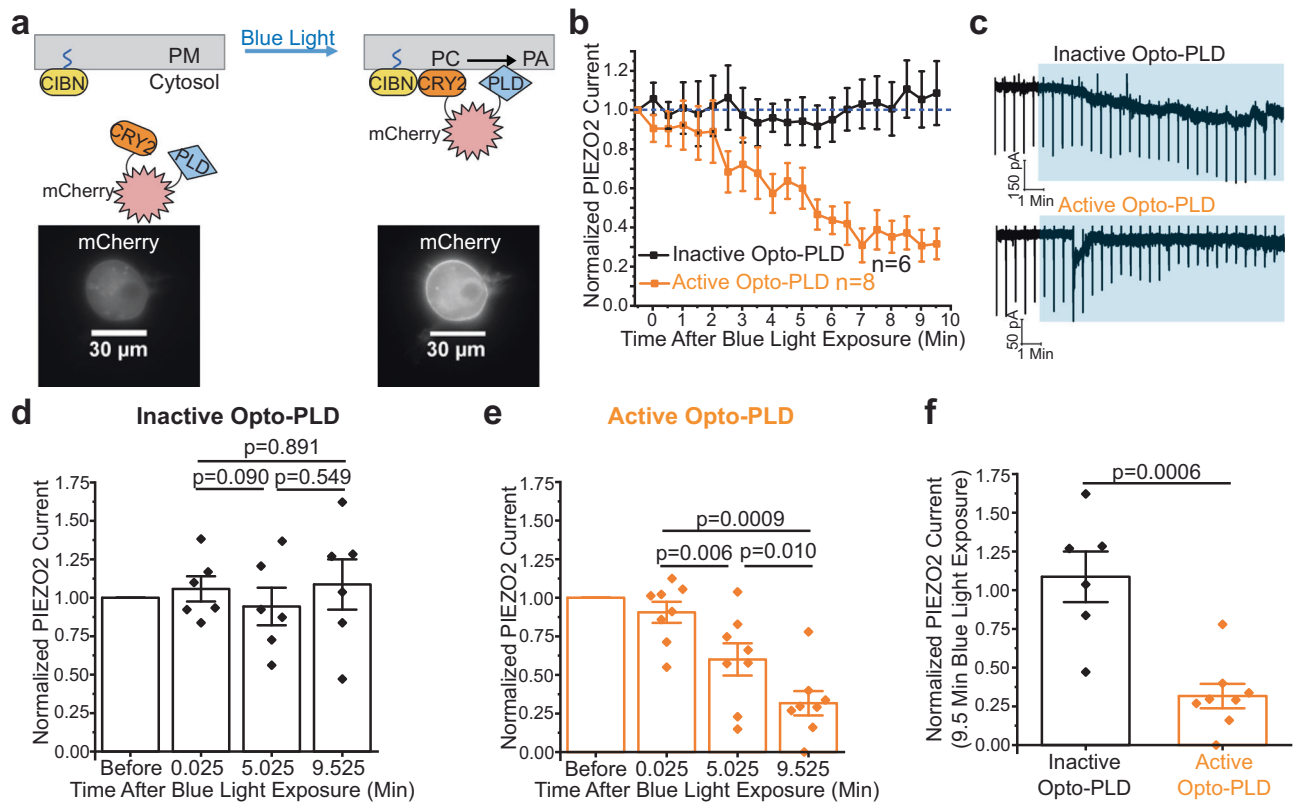
Fig. 5 | Optogenetic activation of PLD inhibits PIEZO2. Whole-cell patch-clamp experiments at −60 mV in N2A-Pz1-KO cells transfected with PIEZO2-GFP and active Opto-PLD (orange, $n = 8$ cells) or inactive Opto-PLD (black; H170A, $n = 6$ cells) as described in the methods section. a Scheme of blue light activation of the Opto-PLD system (Created with BioRender.com) with representative images for mCherry fluorescence (60x) before and after blue light exposure. b PIEZO2-GFP currents with fixed, continuous membrane indentations after blue light exposure normalized to currents before blue light. c Representative current traces. Blue shaded area indicates blue light exposure. Downward deflections indicate mechanically activate

PIEZO2 currents. d Normalized PIEZO2-GFP currents co-expressed with inactive Opto-PLD after blue light exposure (Repeated-Measures ANOVA, $F = 0.365$, df = 2,10, $p = 0.702$; paired two-tailed t-tests displayed). e Normalized PIEZO2-GFP currents co-expressed with active Opto-PLD after blue light exposure (Repeated-Measures ANOVA, $F = 21.386$, df = 2,14, $p = 5.546 \times 10^{-5}$; paired two-tailed t-tests displayed). f Normalized PIEZO2-GFP currents with inactive or active Opto-PLD after 9.5 min of blue light exposure (two-tailed t-test). Figure 5/panel a created with BioRender.com released under a Creative Commons Attribution-NonCommercial-NoDerivs 4.0 International license. All bar graphs are plotted with scatter and mean ± SEM.

Overall, these data indicate that basal PLD activity modulates PIEZO2 channels in DRG neurons, and mechanical sensitivity in vivo.

Discussion

PIEZO1 and PIEZO2 are mechanically activated non-selective cation channels and they play roles in a wide variety of physiological functions. Despite their biomedical importance, no endogenous or exogenous small molecule inhibitor has been identified so far that selectively inhibits PIEZO2 over PIEZO1. Here we build on our earlier work showing that co-expression of the TMEM120A protein inhibits PIEZO2, but not PIEZO1, and we identify phosphatidic acid and LPA as endogenous inhibitors of PIEZO2. We also find that phosphatidic acid generated by PLD enzymes inhibits PIEZO2, but not PIEZO1, thus we identify the PLD pathway as a regulator of PIEZO2 activity.

PIEZO1 and PIEZO2 share a similar structure of a propeller-shaped trimer, with 38 transmembrane segments in each subunit[32]. The membrane footprint of PIEZO proteins is larger than that of any other known ion channel, implying that membrane lipids could greatly influence their behavior. However, research on the impact of membrane lipids on PIEZO channel function is still in the early stages. Various dietary fatty acids have been shown to modulate the activity of both PIEZO1 and PIEZO2 channels, but only one of those lipids showed selectivity for PIEZO1 over PIEZO2: docosahexaenoic acid increased the function of PIEZO1[33] but not PIEZO2[31]. The dietary saturated fatty acid margaric acid (C17:0) has been shown to inhibit both PIEZO1 and PIEZO2 activity, with a higher potency on PIEZO1[18,33]. Linoleic acid

(C18:2), an unsaturated dietary fatty acid on the other hand was shown to increase the activity of both PIEZO1 and PIEZO2[31,33]. The poly-unsaturated fatty acid eicosapentanoic acid (EPA, 20:5) decreased the inactivation time constant for wild-type and gain of function mutant PIEZO1[33] and PIEZO2 channels[34]. The sphingomyelinase enzyme has been reported to alter PIEZO1's inactivation kinetics in vascular endothelial cells by producing ceramides[35].

Recent computational studies using coarse-grained simulation of PIEZO1 and PIEZO2 proteins in a lipid membrane similar in composition to mammalian plasma membranes found that negatively charged membrane lipids are enriched in the vicinity of the propeller-shaped arms of the PIEZO proteins[36–38]. These lipids include phosphatidic acid, phosphatidylserine, phosphatidylinositol, and phosphatidylinositol phosphates. Other studies on PIEZO1 also concluded that phosphatidylinositol 4,5-bisphosphate [PI(4,5)P$_2$] is enriched in the vicinity of the PIEZO arms[39,40], which is not surprising, given a large number of positively charged residues in the cytoplasm inner membrane interface of both channels. Depletion of PI(4,5)P$_2$ by Ca^{2+}-induced activation of phospholipase C (PLC) enzymes upon TRPV1 channel activation has been shown to inhibit PIEZO1 and PIEZO2[41]. Dephosphorylation of PI(3,5)P$_2$ by the phosphoinositide phosphatase myotubularin-related protein-2 was also reported to reduce PIEZO2 activity[42].

All computational studies found multiple potential binding sites for negatively charged lipids, with most sites binding several lipids with varying predicted affinity and similar, yet not identical sites among the different studies. The potential complexity of lipid
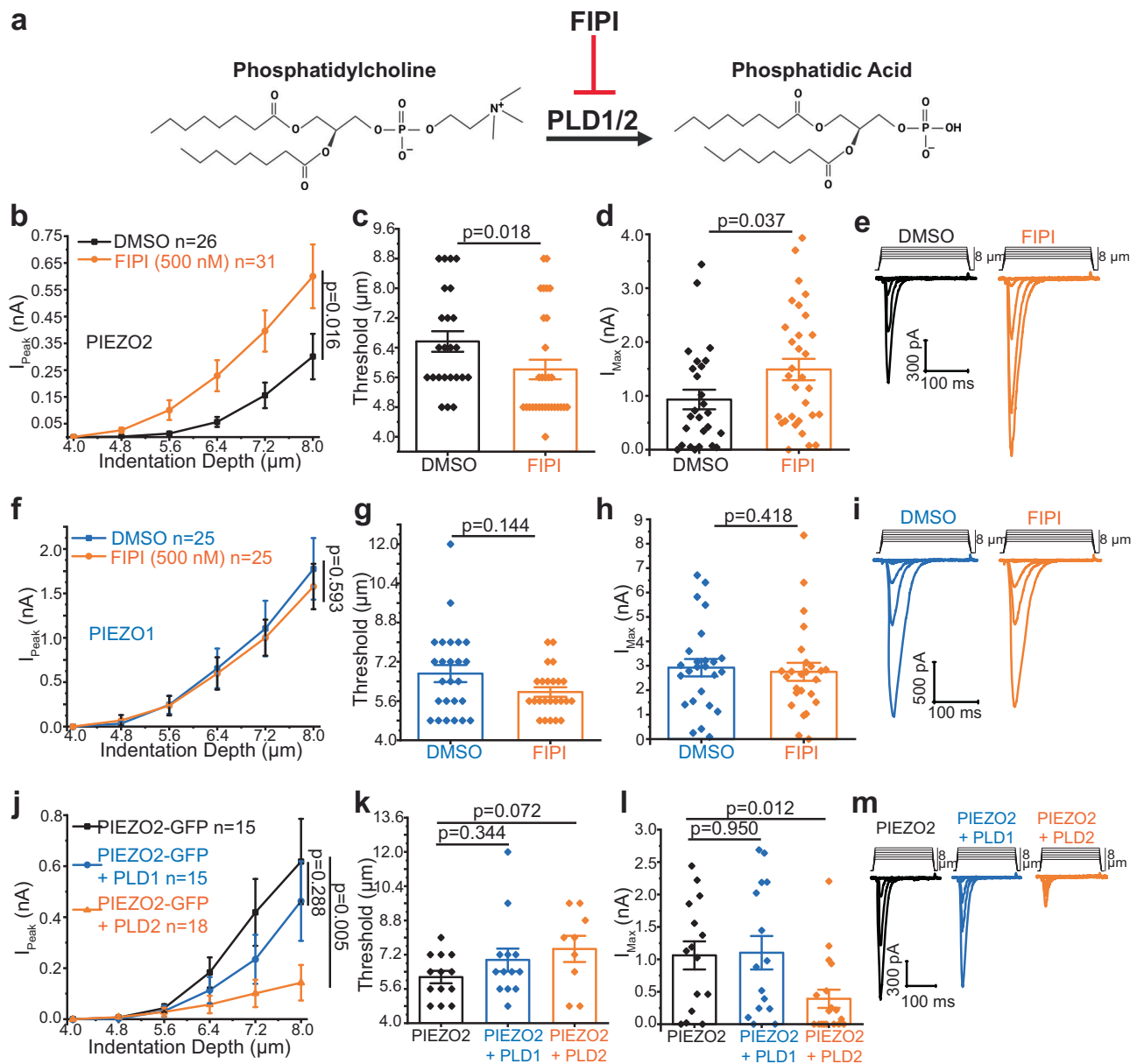
Fig. 6 | Phospholipase D (PLD) negatively regulates PIEZO2 but not PIEZO1.
Whole-cell patch-clamp experiments at −60 mV in transiently transfected N2A-Pz1-KO cells as described in the methods section. **a** Scheme of PLD inhibition by FIPI. **b–e** N2A-Pz1-KO cells transiently transfected with PIEZO2-GFP and were treated with DMSO (black, $n = 26$ cells) or 500 nM FIPI (orange, $n = 31$ cells) for 30 min, see methods for details. **b** Current amplitudes are plotted (mean ± SEM) and the statistical difference of AUC for 4.0–8.0 μm stimuli is calculated with the two-tailed Mann–Whitney test. **d** Membrane indentation depth threshold to elicit mechanically activated current (two-tailed Mann–Whitney). Mechanical threshold is only quantifiable for cells where membrane indentation elicited current, thus non-responding cells reduce the n for DMSO-treated cells to $n = 24$ cells and for FIPI-treated cells to $n = 30$ cells. **d** Maximum current amplitudes (two-tailed Mann–Whitney). **e** Representative current traces. **f–i** N2A-Pz1-KO cells transiently transfected with PIEZO1-GFP treated with 500 nM FIPI (orange, $n = 25$ cells) for 30 min or the vehicle DMSO (blue, $n = 25$ cells) for 30 min. **f** Current amplitudes are plotted (mean ± SEM) and the statistical difference of AUC for 4.0–8.0 μm stimuli is calculated with the two-tailed Mann–Whitney test. **g** Membrane indentation depth

threshold to elicit mechanically activated currents (two-tailed Mann–Whitney). Mechanical threshold is only quantifiable for cells where membrane indentation elicited current, thus non-responding cells reduce the n for FIPI-treated cells to $n = 24$ cells. **h** Maximum current amplitudes (two-tailed Mann–Whitney).
i Representative current traces. **j–m** N2A-Pz1-KO cells transiently transfected with PIEZO2-GFP alone (black, $n = 12$ cells), or together with PLD1 (blue), or PLD2 (orange). **j** Current amplitudes are plotted (mean ± SEM) and the statistical difference of AUC for 4.0–8.0 μm stimuli calculated was with the two-tailed Mann–Whitney test. **k** Membrane indentation depth threshold to elicit mechanically activated current (Kruskal–Wallis, $\chi^2 = 3.298$, df = 2, $p = 0.0192$; two-tailed Mann–Whitney tests displayed). The mechanical threshold is only quantifiable for cells where membrane indentation elicited current, thus non-responding cells reduce the n for PIEZO2-GFP alone cells to $n = 13$ cells, for PIEZO2-GFP + PLD1 cells to $n = 13$ cells, and for PIEZO2-GFP + PLD2 cells to $n = 9$ cells. **l** Maximum current amplitudes (Kruskal–Wallis, $\chi^2 = 7,906$, df = 2, $p = 0.0192$; two-tailed Mann–Whitney tests displayed). **m** Representative current traces. All bar graphs are plotted with scatter and mean ± SEM.
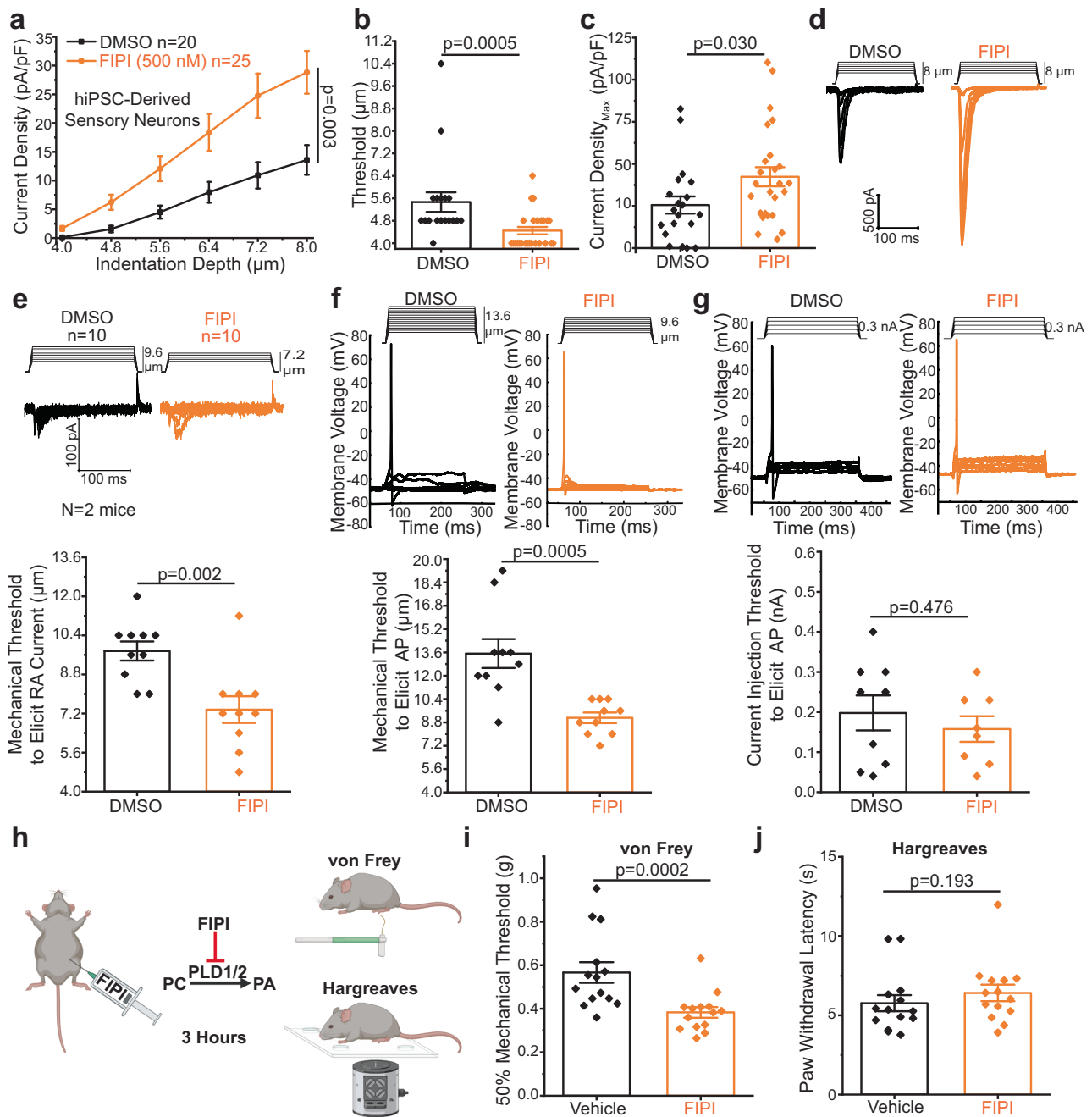
Fig. 7 | PLD modulates native rapidly adapting mechanically activated currents in peripheral sensory neurons. a–**d** Whole-cell patch-clamp at −60 mV in hiPSC-sensory neurons treated with 500 nM FIPI (orange, $n = 25$ cells) or DMSO (black, $n = 20$ cells) for 30 min as described in the methods section for details. **a** Current densities are plotted (mean ± SEM) and the statistical difference of AUC for 4.0–8.0 μm stimuli is calculated with the two-tailed Mann−Whitney test. **b** Membrane indentation depth thresholds to elicit mechanically activated current (two-tailed Mann−Whitney). Mechanical threshold is only quantifiable for cells where membrane indentation elicited current, thus non-responding cells reduce the n for DMSO-treated cells to $n = 18$ cells. **c** Maximum current densities (two-tailed Mann−Whitney). **d** Representative current traces. **e** Whole-cell patch-clamp at −60 mV in isolated mouse DRG neurons treated with DMSO (black, $n = 10$ cells) or FIPI (orange, $n = 10$ cells) as described in the methods section. Representative current traces (top), and membrane indentation depth thresholds to elicit mechanically activated RA currents (bottom) (two-tailed t-test). **f**–**g** Whole-cell

current-clamp in isolated mouse DRG neurons treated with DMSO (black, $n = 10$ cells) or FIPI (orange, $n = 10$ cells) for 30 min as described in the methods section. **f** Representative traces (top), and membrane indentation depth threshold to elicit an action potential (bottom) (two-tailed t-test). **g** Representative traces (top), and current injection threshold to elicit an action potential (bottom) (two-tailed t-test) in the same cells used in panels **e** and **f**. In three cells the seal was lost before current injections could be performed. **h**–**j** Mechanical testing using Von Frey filaments and thermal testing using the Hargreaves apparatus were performed on mice receiving an I.P. injection of 3 mg/kg FIPI ($n = 14$ mice) or vehicle ($n = 14$ mice) as described in the methods section. **h** Experimental design (created with BioRender.com). **i** von Frey testing 50% mechanical threshold (two-tailed Mann−Whitney). **j** Hargreaves paw withdrawal latency (two-tailed Mann−Whitney). Figure 7/panel h was created with BioRender.com released under a Creative Commons Attribution-NonCommercial-NoDerivs 4.0 International license. All bar graphs are plotted with scatter and mean ± SEM.

interactions with PIEZO2 makes it hard to pinpoint potential binding sites on the channel, and further studies will be required to identify lipid binding sites responsible for the effect of phosphatidic acid and LPA.

The lipids we identified that inhibit PIEZO2 channels, phosphatidic acid, and LPA, both have a free phosphate group attached to the glycerol backbone. The only difference between these lipids is the presence of one vs. two acyl chains (LPA vs. phosphatidic acid, respectively). In our experiments, phosphatidic acid and LPA were sufficient to inhibit PIEZO2 channels indicating that the number of acyl chains is not a major determinant of the inhibitory effect. The degree of unsaturation and length of LPA's acyl-chain did not grossly affect LPA's inhibition of PIEZO2. While we did not perform similar experiments with phosphatidic acid due to solubility constraints, it is likely that phosphatidic acid species with unsaturated acyl-chains also inhibit PIEZO2 as PLD enzymes generate phosphatidic acid from phosphatidylcholine already present in the cellular membrane which is comprised of diverse tail lengths and degrees of unsaturation[43]. The free phosphate attached to the glycerol backbone, on the other hand, is important for PIEZO2 inhibition as phosphatidylglycerol and phosphatidylserine in which glycerol or serine are attached to the phosphate, did not inhibit the channel.

We identified phosphatidic acid and LPA as inhibitors of PIEZO2 by dissecting the mechanism of inhibition by TMEM120A. TMEM120A (a.k.a.TACAN) was proposed to be a component of slowly adapting mechanically activated ion channels responsible for mechanical pain[9]. This proposal was based on the appearance of mechanically activated currents in cells transfected with TMEM120A, and on the finding that siRNA knockdown of TMEM120A reduced the proportion of slowly adapting mechanically activated currents in DRG neurons. These findings however were not reproduced by other laboratories[8,10–13,22], raising doubts about TMEM120A functioning as a mechanically activated channel. Structural studies[10,12,13,22,44] indicated that TMEM120A shares structural homology with the long-chain fatty acid elongase enzyme ELOVL7[14]. Other studies indicated that TMEM120A is involved in adipocyte differentiation[45], triglyceride production[45], and its genetic deletion from adipocytes resulted in lipodystrophy in mice[46]. These studies indicated that TMEM120A is located in the nuclear envelope, and suggested that its effect on adipocytes was mediated by affecting the expression of other genes, see our recent review on TMEM120A for further discussion[16]. Our data show that TMEM120A overexpression increases intermediates in the Kennedy pathway of triglyceride synthesis. It will require further studies if this effect is due to an enzymatic activity of TMEM120A, or modifying expression of other genes. Our primary goal here was to take advantage of the selective inhibition of PIEZO2 by TMEM120A and identify potential channel inhibitor molecules. Thus, we focused on the two lipids that showed the most robust increase in TMEM120A-expressing cells, phosphatidic acid and LPA, and found that intracellular application of either of these lipids inhibited PIEZO2, but not PIEZO1.

Phosphatidic acid, other than being an intermediate of triglyceride synthesis in the Kennedy pathway, can also be generated by phospholipase D (PLD) enzymes that cleave the headgroup from phospholipids, mainly phosphatidylcholine, leaving the phosphate on the glycerol backbone and thus generating phosphatidic acid. Phosphatidic acid has been thoroughly studied in plant hormonal signaling[47], and has been implicated in modulating cellular processes such as membrane traffic, endocytosis, and exocytosis in mammals, but its precise role in these processes is not well defined[48]. There have also been sporadic reports on phosphatidic acid affecting ion channels[49,50], but this lipid has been understudied in mammalian signaling compared to phosphoinositides and DAG. Specifically, PLD2 has been implicated in the positive regulation of mechanosensitive TREK-1 channels[50]. Given that TREK-1 is a mechanically activated hyperpolarizing channel, which is positively regulated by PLD2, one may argue

that TREK channel modulation contributes to the effects of FIPI in modulating mechanosensitivity in current-clamp and behavioral experiments. Our findings that neither resting membrane potential nor current injection threshold was different in FIPI-treated and control neurons, however, argue against the involvement of TREK-1 in the effects of FIPI on mechanically induced electrical activity and mechanosensitivity in behavioral experiments.

LPA, besides being an intermediate in the Kennedy pathway of triglyceride synthesis, is also well known as an extracellular signaling molecule, acting on cell surface receptors. Extracellular LPA is generated by either PLA1/2 enzymes hydrolyzing extracellularly facing PA, or by conversion of lysophosphatidylcholine (also produced by PLA1/2) to LPA by autotaxin enzymes[51]. Extracellular LPA is thought to be generated by these enzymatic reactions on the extracellular surface of the plasma membrane[51], and it is unlikely that LPA generated inside the cell crosses the plasma membrane in sufficient quantities to serve as an extracellular signal[52]. LPA has also been reported to activate TRPV1 and TRPA channels via direct binding[53,54].

PLD enzymes generate phosphatidic acid by removing the headgroup of phosphatidylcholine (Fig. 5a). There are two PLD enzymes in mammals. PLD2 is thought to have constitutive activity, while PLD1 is tightly regulated by a variety of factors including the small G-proteins Arf and Rho, as well as Protein Kinase C (PKC)[30]. PLD-s are involved in a variety of cellular functions, including cell metabolism, migration, and exocytosis[30]. Even though both PLD-s are expressed in DRG neurons[55–57], the role of PLD enzymes in somatosensory physiology, and specifically in the regulation of PIEZO2 channels, is completely unexplored. Here we show that optogenetic activation of PLD inhibits PIEZO2, but not PIEZO1, demonstrating that in principle, PLD activity can influence PIEZO2 channel activity. We also find that the PLD inhibitor FIPI increases mechanically activated PIEZO2, but not PIEZO1 currents, indicating that basal PLD activity modulates PIEZO2 activity. PLD inhibition by FIPI also increased the amplitudes of endogenous rapidly adapting mechanically activated currents in hiPSC-derived peripheral sensory neurons and reduced the mechanical threshold for action potential firing in mouse DRG neurons that had rapidly adapting mechanically activated currents. Consistent with these data FIPI injection decreased the mechanical threshold in experiments using von Frey filaments, a behavioral assay that was shown to be dependent on PIEZO2 channels[58].

In conclusion, we show that phosphatidic acid and LPA inhibit PIEZO2, but not PIEZO1 activity, and identify the PLD pathway as a modulator of PIEZO2 channels and mechanical sensitivity in mice. The specific inhibition of PIEZO2 over PIEZO1 by phosphatidic acid and LPA may serve as a basis for future work to identify clinically useful specific PIEZO2 inhibitors.

Methods

Animals
All animal procedures were approved by the Institutional Animal Care and Use Committee at Rutgers New Jersey Medical School. Mice were kept in a barrier facility under a 12/12 h light/dark cycle, 72–74 °F, and 60–64% humidity. Adult (8–12 weeks old) wild-type C57BL/6 mice (The Jackson Laboratory) of both sexes were used for both experiments.

Cell lines
Neuro2A-*Piezo1*-KO (N2A-Pz1-KO) cells in which endogenous *Piezo1* was deleted using CRISPR were a kind gift from Drs. Valeria Vasquez and Gary Lewin. These cells were cultured in Dulbecco's Modified Eagle Medium/F-12 (HAM) supplemented with 1% penicillin-streptomycin and 10% FBS at 37 °C with 5% CO_2. These cells were transiently transfected with plasmids as described below using either Effectene (Qiagen, Cat. # 301425) or PEI-Max (Polysciences Inc, Cat. # 24765-100). For whole-cell electrophysiology and TIRF experiments, these cells were

split onto poly-L-lysine coated glass coverslips 24 h after transfection and used for experiments 48 total hours after transfection. hiPSC-derived peripheral sensory neurons (RealDRG™) were differentiated and cultured according to the manufacturer's (Anatomic Incorporated) instructions (briefly described below) before whole-cell patch clamp experiments.

Lipidomic LC-MS/MS analysis

N2A-Pz1-KO cells cultured in 35 mm diameter dishes were transfected using PEI-Max (Polysciences Inc, Cat. # 24765-100) with 1500 ng ptdTomato-N1 vector, 1500 ng TMEM120A-Tom, or 1500 ng TMEM120B. Each group was comprised of three independent transfections (9 total transfections). The cells were harvested 48-h after transfection and counted via hemocytometer. One million cells from each independent transfection were collected and centrifuged. The cell pellets were washed with ice-cold PBS and resuspended in 500 μL of extraction buffer (0.05 M HCl, 49% methanol, 1% SPLASH Lipidomic Mass Spec Standard [Avanti Polar Lipids, Cat. # 330707]), and 1 mL methyl-tert-butyl-ether was added. Samples were vortexed for 30 s, and 600 μL of the organic layer was transferred to a new tube. Samples were allowed to dry overnight and stored at −80 °C.

The reversed-phase separation was performed on a Vanquish Horizon UHPLC system (Thermo Fisher Scientific, Waltham, MA) with a Poroshell 120 EC-C18 column (150 mm × 2.1 mm, 2.7 μm particle size, Agilent InfinityLab, Santa Clara, CA) using a gradient of solvent A (90%:10% H_2O:MeOH with 34.2 mM acetic acid, 1 mM ammonium acetate), and solvent B (75%:25% IPA:methanol with 34.2 mM acetic acid, 1 mM ammonium acetate). The gradient was 0 min, 25% B; 2 min, 25% B; 5.5 min, 65% B; 12.5 min, 100% B; 19.5 min, 100% B; 20.0 min, 25% B; 30 min, 25% B. The flow rate was 200 μL/min. The injection volume was 5 μL, the column temperature was 55 °C, and the autosampler temperature was set to 4 °C. The full scan mass spectrometry analysis was performed on a Thermo Q Exactive PLUS with a HESI source which was set to a spray voltage of −2.7 kV under negative mode and 3.5 kV under positive mode. The sheath, auxiliary, and sweep gas flow rates of 40, 10, and 2 (arbitrary unit) respectively. The capillary temperature was set to 300 °C and the aux gas heater was 360 °C. The S-lens RF level was 45. The m/z scan range was set to 100 to 1200 m/z under both positive and negative ionization modes. The AGC target was set to 1e6 and the maximum IT was 200 ms. The resolution was set to 140,000 at m/z 200. The lipidomic annotation and quantitation were performed using MS-DIAL[59,60]. The accurate mass tolerance settings were 0.005 (MS1) and 0.05 (MS2). The acquisition software used was Xcalibur (ThermoFisher Scientific). The lipid annotation was based on the MS-DIAL built-in database, and the identification score cutoff was set to 80. The ion counts were normalized to the SPLASH internal standard. All samples were run on the same day to ensure comparability.

For the calculation of total LPA (0), PA (0), DG (0), and TG (0) in Fig. 1, the total ion counts of 5 LPA, 9 PA, 8 DG, and 13 TG species were summed. The same method is applied when calculating the total LPA (1), LPA (2-6), PA(1), PA(2-12), DG(1), DG(2-5), TG(1) and TG(2-18) levels for Supplementary Fig. 1. The values for individual lipids are presented in the Source Data file. All raw data files pertaining to LC-MS/MS experiments have been deposited to the Metabolomics WorkBench repository under study ID ST003090.

Fluorometric determination of total LPA/PA

N2A-Pz1-KO cells cultured in 60 mm diameter dishes were transfected using PEI-Max with 5 μg ptdTomato-N1 vector (mock), 5 μg TMEM120A-WT-Tom, 5 μg TMEM120A-W193A-Tom, or 5 μg TMEM120A-AxxAA-Tom. Each group was comprised of 6 independent transfections except TMEM120A-AxxAA-Tom which was comprised of 5 independent transfections (23 total transfections). Cells were harvested 48-h after transfection and counted using a hemocytometer. Four million cells per sample were collected and centrifuged. Cell

pellets were washed with ice-cold PBS, and resuspended in 500 μL of extraction buffer (0.05 M HCl, 50% methanol), and 1 mL methyl-tert-butyl-ether was added. Samples were vortexed for 30 s, and 800 μL of the organic layer was transferred to a new tube. Samples were allowed to dry overnight. Once dry the next day, the Total Phosphatidic Acid Assay Kit (Cell Bio Labs, Inc. Cat. # MET-5019) was used following the manufacturer's instructions. Briefly, dried lipid extracts were resuspended in 50 μL of assay buffer and 10 μL of experimental samples or 1 mM phosphatidic acid standards (to generate a standard curve) were added to a 96-well plate. 40 μL of lipase solution was added to each sample, and the plate was incubated at 37 °C for 30 min. This step hydrolyzes LPA and phosphatidic acid producing glycerol-3-phosphate and free fatty acid. Next, 50 μL of glycerol-3-phosphate oxidase in the presence of a fluorometric probe was added to each sample and allowed to incubate at room temperature for 10 min. This step oxidizes the glycerol-3-phosphate generating H_2O_2 and dihydroxyacetone phosphate. The H_2O_2 interacts with the fluorometric probe producing fluorescence. The fluorescence was measured using the 96-well plate reader FlexStation 3 (Molecular Devices) using 545 nm excitation and 590 nm emission wavelengths. The total LPA/PA concentrations were calculated using the linear equation from the standard curve generated by standards provided by the manufacturer.

Whole-cell patch clamp

Whole-cell patch-clamp recordings were performed at room temperature (22–24 °C) as previously described[41]. Briefly, patch pipettes were prepared from borosilicate glass capillaries (Sutter Instrument, Cat. # BF150-75-10) using a P-97 pipette puller (Sutter Instrument) and had a resistance of 2.0–7.0 MΩ. After forming GΩ-resistance seals, the whole-cell configuration was established. All electrophysiology recordings were performed with an Axopatch 200B amplifier (Molecular Devices) and pClamp 11.2. Currents were filtered at 5 kHz using a low-pass Bessel filter of the amplifier and digitized using a Digitata 1440 unit (Molecular Devices). All voltage-clamp measurements were performed at a holding voltage of −60 mV. For all current-clamp measurements, cells that had a resting membrane potential more positive than −40 mV were excluded.

All measurements were performed using an extracellular solution containing 137 mM NaCl, 5 mM KCl, 1 mM $MgCl_2$, 2 mM $CaCl_2$, 10 mM HEPES, and 10 mM glucose (pH adjusted to 7.4 with NaOH). The patch pipette solution for voltage-clamp (in heterologous systems) and current-clamp measurements contained 140 mM K-gluconate, 1 mM $MgCl_2$, 2 mM Na_2ATP, 5 mM EGTA, and 10 mM HEPES (pH adjusted to 7.3 with KOH). For mechanically activated voltage-clamp measurements in DRG neurons, the following cesium-based solution was used: 133 mM CsCl, 1 mM $MgCl_2$, 1 mM $CaCl_2$, 5 mM EGTA, 4 mM Na_2ATP, 10 mM HEPES (pH adjusted to 7.3 with CsOH).

Mechanically activated currents were measured from N2A-Pz1-KO cells transiently transfected with 500 ng/cDNA construct using Effectene (Qiagen, Cat. # 301425), isolated mouse DRG neurons, and hiPSC-derived peripheral sensory neurons (Anatomic Incorporated, Cat. # 1020F1-1M) as previously described[41]. Briefly, mechanical stimulation was performed using a heat-polished glass pipette (tip diameter about 3 μm) controlled by a piezoelectric crystal drive (Physik Instrumente) positioned at 60° to the surface of the cover glass. The probe was positioned so that 10-μm movement did not visibly contact the cell but an 11.5-μm stimulus produced an observable membrane deflection. Cells received a membrane indentation lasting 200 ms at a depth of 4.0 Δ + 0.8 μm/10 s. For measurements using Opto-PLD (AddGene, Active Opto PLD Cat. # 140114, Inactive Opto-PLD Cat # 140061), an indentation depth that produced consistent and sub-maximal current was applied to the cells every 30 s. To reach an intensity of blue light sufficient to activate the Opto-PLD system, an LED light source (CoolLED, pE-300) and 60x oil objective (N.A.: 1.49) were used. Measurements from cells that showed significant swelling after repetitive

mechanical stimulation or had substantially increased leak current were discarded. Only one set of membrane indentation protocols was performed per cell (i.e., each data point displayed is from a unique patch-clamped cell). All experiments utilizing transient transfections are comprised of a minimum of 2 independent transfections. All experiments utilizing isolated mouse DRG neurons are comprised of preparations from a minimum of 2 mice. Experiments utilizing hiPSC-derived peripheral sensory neurons were performed with 3 unique vials of cells provided by Anatomic Incorporated.

For the intracellular application of lipids, the patch pipette solution described above was supplemented with the denoted lipid. Once the whole-cell configuration was established, we waited 5 min for lipids to dialyze into the cell before measurements were taken. Patch pipettes used for these experiments had a resistance of 2.0–3.5 MΩ to ensure the opening was wide enough to allow for sufficient dialysis of lipids. Patch pipette solution was used as a solvent for dioctanoyl-phosphatidic acid (Avanti Polar Lipids, Cat. # 830842P), palmitoyl-LPA (Cayman Chemical, Cat. # 10010094), stearoyl-LPA (Avanti Polar Lipids, Cat. # 857128 P), oleoyl-LPA (Cayman Chemical, Cat. # 62215), linoleoyl-LPA (Cayman Chemical, Cat. # 38309), dioctanoyl-PG (Avanti Polar Lipids, Cat. # 840433P), dioctanoyl-PS (Avanti Polar Lipids, Cat. # 840031P), and palmitoyl-CoA (MilliporeSigma, Cat. # P9716) in these experiments.

For the extracellular application of dioctanoyl-phosphatidic acid, the solvent used was an extracellular patch-clamp solution containing 137 mM NaCl, 5 mM KCl, 1 mM MgCl$_2$, 2 mM CaCl$_2$, 10 mM HEPES, and 10 mM glucose (pH adjusted to 7.4 with NaOH). These cells were probed with increasing membrane indentation depths to determine an appropriate stimuli strength that produced consistent, sub-maximal mechanically activated currents. The cells were continuously indented with this depth every 30 s for 2 min in the absence of any lipids, dioctanoyl-phosphatidic acid (300 μM) was perfused for 8 min, and then a wash step was performed for 2 min. For the extracellular application of palmitoyl-ccPA (Cayman Chemical, Cat. # 10010293), DMEM/F-12 (HAM) was used as the solvent. Cells were cultured for 24 h in the lipid-supplemented media before electrophysiological measurements were taken.

For pharmacological inhibition of PLDs, cells were incubated in DMEM/F-12 (HAM) containing 500 nM FIPI (Cayman Chemical, Cat. # 13563) or an equivalent volume of DMSO (0.005%) for 30 min and were patched in extracellular solution containing 500 nM FIPI. To inhibit GPAT, cells were incubated overnight with media supplemented with 100 μM FSG67 (Focus Biomolecules, Cat. # 10-4577) or the equivalent volume of DMSO (0.1%).

Data were collected and analyzed in Clampfit 11.2 software including the quantification of peak current amplitudes for each indentation depth. To compare the peak current amplitude data for the indentation depth range where the majority of cells survived (4.0–8.0 μm), area under the curve (AUC) calculations were made in Origin 2021. The AUC for these indentation depths was calculated for each cell using the peak current amplitudes elicited through 4.0–8.0 μm indentation depths. The AUC values were compared between groups to evaluate any statistical differences for these stimulations.

The inactivation time constant (tau) for mechanically activated currents was measured in Clampfit 11.2 software by fitting an exponential decay function. We used the currents evoked by the third stimulation after the threshold in most experiments. Except in the cells where only the two largest stimuli evoked a current, in which case we measured the tau using the largest stimulus (provided it reached 40 pA).

DRG neurons

DRG neurons were isolated as previously described[41]. Briefly, mice were anesthetized with an i.p. injection of ketamine (100 mg/kg) and xylazine (10 mg/kg) and perfused via the left ventricle with ice-cold Hank's Buffered Salt Solution (HBSS). DRGs were harvested from all spinal segments after laminectomy and removal of the spinal column

and maintained in ice-cold HBSS for the duration of the isolation. Isolated ganglia were cleaned from excess nerve tissue and incubated with type 1 collagenase (3 mg/mL) and dispase (5 mg/mL) in HBSS at 37 °C for 30 min, followed by mechanical trituration. Digestive enzymes were then removed after centrifugation of the cells at 100 g for 5 min. Isolated DRG neurons were resuspended in warm DMEM/F-12 (1% penicillin-streptomycin and 10% FBS) and plated onto glass coverslips coated with poly-L-lysine (MilliporeSigma, Cat. # P4707) and laminin (MilliporeSigma, Cat. # L2020).

For overnight incubation with palmitoyl-ccPA (Cayman Chemical, Cat # 10010293), the DRG neurons were allowed to fully adhere to the glass coverslips before the media was replaced with fresh media or fresh media containing 300 μM palmitoyl-ccPA for 24–32 h. DMEM/F-12 (1% P/S and 10% FBS) was used as the solvent for the palmitoyl-ccPA. The DRG neurons were incubated with palmitoyl-ccPA for 24 h before whole-cell electrophysiology experiments. For experiments using FIPI, DRG neurons were used between 24–48 h after isolation. The neurons were incubated in media containing 500 nM FIPI or the equivalent volume of DMSO (0.005%) for 30 min, and cells were patched in an extracellular solution containing 500 nM FIPI.

Mechanically activated currents from DRG neurons were categorized by their inactivation kinetics as rapid, intermediate, or slow based on the criteria from our previous publications[8,41,61]. We considered currents to be rapidly adapting if they were fully inactivated before the end of the 200-ms mechanical stimulus. The inactivation time constants (tau) of these currents were 14.16 ± 5.12 ms (mean ± SD) similar to our previous work[8,41,61]. This inactivation time constant was very similar to PIEZO2 transiently transfected in N2A-P1KO cells (Supplementary Fig. 4a, c, e–i and Supplementary Fig. 8b, c). Intermediately adapting currents did not fully inactivate but the leftover current at the end of the mechanical stimulation was <50% of the peak current. The inactivation time constant for these currents was 30.67 ± 10.70 ms. Slowly adapting currents also did not fully inactivate, and the leftover current at the end of the mechanical stimulation was >50% of the peak current. The inactivation constant for these currents was 111.85 ± 52.47 ms.

hiPSC-derived sensory neurons

hiPSC-derived sensory neurons (RealDRG^{TM}, Anatomic Incorporated, Cat. # 1020F1-1M) were cultured and differentiated according to manufacturers (Anatomic Incorporated) instructions. Briefly, hiPSC cells stored in liquid N$_2$ were thawed and plated onto poly-L-ornithine (MilliporeSigma, Cat. # P4967) and iMatrix-511 SILK (Anatomic Incorporated, Cat. # M511S) coated 12 mm coverslips. Cells were cultured in differentiation Chrono Senso-MM media (Anatomic Incorporated, Cat. # 7008) with no antibiotics present for 12–16 days. Media was changed every 48 h. The hiPSC-derived neurons were incubated in media containing 500 nM FIPI or the equivalent volume of DMSO (0.005%) for 30 min and were patched in an extracellular solution containing 500 nM FIPI.

TIRF microscopy

N2A-Pz1-KO cells were transiently transfected with cDNA encoding *Piezo2-GFP* and *Tmem120a-tdTomato*, *Tmem120a*- W193A-*tdTomato*, *Tmem120a-tdTomato* (AxxAA) or *tdTomato* (500 ng/construct, Effectene). The next day, the cells were plated onto poly-L-lysine coated 25 mm round coverslips (#1.5 thickness; ThermoFisher Scientific). The cells were used for TIRF imaging two days after transfection. Coverslips were placed into a recording chamber filled with extracellular solution (137 mM NaCl, 5 mM KCl, 1 mM MgCl$_2$, 2 mM CaCl$_2$, 10 mM HEPES, and 10 mM glucose, pH adjusted to 7.4 with NaOH). TIRF images were obtained at room temperature using a Nikon Eclipse Ti2 microscope. Fluorescence excitation was performed using a 15 mW solid state 488 and 561 nm laser at 90% of the maximal power through a CFI Aprochromat TIRF 60X oil objective (N.A.: 1.49). Images were

captured using an ORCA-Fusion Digital CMOS camera (Hamamatsu) through emission filters 525/50 and 600/50 nm for the green and red channels, respectively.

The images were analyzed using Nikon NIS-Elements AR Analysis software. Regions of interest (ROIs) were generated by hand drawing the outline of individual cells allowing for analysis of fluorescent signal over the total area of each cell in the TIRF angle. Mean fluorescence intensities within these single-cell ROIs were averaged for each coverslip (5–32 total cells/coverslip) and plotted.

Behavioral testing

Experiments were performed on male and female mice (C57Bl/6 J, The Jackson Laboratory, Bar Harbor, Maine) (age 5–8 weeks; weight 22–25 g). Mice were kept in the Laboratory Animal Housing Faculty of Rutgers New Jersey Medical School at 24–25 °C, provided with standard mouse chow and water ad libitum, and maintained under a 12 h light/dark cycle. Animals were acclimatized to the testing room for at least 1 h before all behavioral tests. The same experimenter handled and tested all animals in each experiment and was blinded to the treatment. We used both male and female mice, and the data pooled together as we did not observe a significant difference between the sexes. FIPI (in DMSO stock) was diluted in a mixture of Kolliphor EL (Sigma-Aldrich, Cat. # C5135) and standard PBS (Gibco) in the ratio 1:1:48 with a final concentration of FIPI 0.5 mg/mL. Mice were intraperitoneally injected with FIPI ($n = 14$) or vehicle ($n = 14$) at the dose of 3 mg/kg with a 0.5 mL Hamilton syringe and 30 g needle and returned to the home cage for 2 h. After drug administration, mice were allowed to acclimatize on a metal mesh platform in an individual Plexiglas chamber for 1 h.

Mechanical sensitivity was assessed by measuring paw withdrawal thresholds to von Frey filament (Stoelting, Wood Dale, IL) stimuli. For determining the 50% withdrawal threshold using the Up-Down method, calibrated von Frey filaments were applied as previously described[62,63] and found in the von Frey Test protocol (Standard Operating Procedure The Jackson Laboratory Mouse Facility). Briefly, testing was initiated by the application of filaments to the soft pad of the hind paw between the tori at the base of the digits for 2–3 sec using the filament force in the mid-range (0.4 g). After a positive response (defined as withdrawal, shaking, splaying, lifting, or licking of the paw), we apply the next lower von Frey filament. If the animal did not respond, we applied the next higher von Frey filament. Four additional measures are recorded after the first change in response for both the left and right paw. The 50% threshold is then calculated using the formula[63]: 50% threshold $(g) = 10^{(X + kd)}$, where $X = $ log10 (target force in grams of the final von Frey filament used), $k = $ tabular value for the response pattern (see Appendix 1 in reference[62] and $d = $ the average increment (in log units) between the target force in grams of the von Frey filaments used (2.0, 1.4, 1.0, 0.6, 0.4, 0.16, 0.07, 0.04 g).

Thermal sensitivity of the paw was assessed with a Model 336 Analgesia Meter (IITC Life Science) as described previously[64]. After performing von Frey mechanical testing mice were transferred and acclimatized on a glass floor in the same Plexiglas chambers for 30 min, after which a light beam was focused on the midplantar region of the hind paw. The latency to respond by withdrawing the paw from the light was recorded. The cutoff time was set up to 20 s to prevent tissue damage. Stimuli were applied to the paws three times at 5 min intervals, and the average latency was calculated[64].

The experimenter for all behavioral experiments was blind to what treatment each mouse received during testing and quantification of the data.

cDNA constructs

The GFP-tagged *Piezo1* construct (PIEZO1-GFP) was generated by subcloning the mouse *Piezo1* to the pcDNA3.1(-) vector from the original IRES-GFP vector then PCR cloning GFP and ligating it to the N-terminus of *Piezo1*[40]. The GFP-tagged *Piezo2* construct (PIEZO2-GFP) was generated by PCR cloning GFP and ligating it to the N-terminus of *Piezo2* in the pCMV SPORT6 vector. The tdTomato-tagged *Tmem120a* construct was generated by PCR cloning *Tmem120a* using the Origene MR205146 clone as a template and subcloning it to the ptdTomato-N1 vector (Clontech), placing the tdTomato tag to the C-terminus of *Tmem120a*[8]. For PCR cloning, the Pfu-Ultra proofreading enzyme (Agilent) was used and the constructs were verified with sequencing. The *Tmem120b* cDNA clone was purchased from Origene (MR205067, NM_001039723). The Opto-PLD active and inactive constructs were purchased from Addgene (140114, and 140061). The hPLD1 cDNA clone was a kind gift from Dr. Michael A. Frohman (Genbank accession number = U3845). The mPLD2 cDNA clone was a kind gift from Dr. Guangwei Du (Genbank accession number = 87557). Point mutations of *Tmem120a* were generated using the QuikChange II XL Site-Directed Mutagenesis Kit (Agilent, Cat. # 200522) per the manufacturer's instructions. Primers for point mutations generated for TMEM120A-W193A (F-acacata atgatggaaaaccgcccagcctttgatcctggaa; R-ttccaggatcaaaggctgggcggtt ttccatcattatgtgt) and TMEM120A-AxxAA (F-ctgacaggaatgtggacaca-taagcagcgaaaaccgcccagcctttgatcctggaaccat; R- atggttccaggatcaaagg ctgggcggttttcgctgcttatgtgtccacattcctgtcag) were purchased from Eton Biosciences. Full plasmid sequencing (Plasmidsaurus) was used to confirm that the intended residues were mutated and that no off-target mutations were present.

Statistics and reproducibility

Data are represented as mean ± SEM plus scatter plots as indicated in figure legends. To determine whether data significantly deviated from a normal distribution, Shapiro–Wilk tests were used. To determine whether data between groups had a significant difference in variance, Levene's test for homogeneity of variance (centered on median) was used. When comparing between groups for data that did not significantly deviate from a normal distribution or variance, statistical significance was calculated either with a two-sample t-test (two-tailed), or ANOVA with post-hoc Tukey test. Between-group comparisons with data that significantly deviated from normality, the non-parametric Mann–Whitney or Kruskal–Wallis tests were used. When comparing groups with repeated measures, a repeated-measures ANOVA & paired-sample t-test for normally distributed data. To compare nominal data (distribution of inactivation kinetics from mouse DRG neurons), a Chi-Square test was used. When multiple comparisons were necessary, the threshold for significance was corrected for the number of comparisons ($\alpha = 0.05$/# of comparisons). The specific tests and sample sizes for each experiment are described in the figure legends and noted in the figures. No statistical method was used to predetermine the sample size. For all electrophysiology experiments, the experimenter chose a group at random to start with at the beginning of the experimental period and then alternated between groups throughout its course. The experimenter for all behavioral experiments was blind to what treatment each mouse received during testing and quantification of the data. All statistical testing was performed using R Commander. Data plotting was performed using the Origin 2021 software.

Reporting summary

Further information on research design is available in the Nature Portfolio Reporting Summary linked to this article.

Data availability

Raw LC-MS/MS files have been deposited to Metabolomics WorkBench repository under study ID ST003090. Source data are provided with this paper.

References

1. Coste, B. et al. Piezo1 and Piezo2 are essential components of distinct mechanically activated cation channels. *Science* **330**, 55–60 (2010).
2. Szczot, M., Nickolls, A. R., Lam, R. M. & Chesler, A. T. The form and function of PIEZO2. *Annu. Rev. Biochem* **90**, 507–534 (2021).
3. Murthy, S. E., Dubin, A. E. & Patapoutian, A. Piezos thrive under pressure: mechanically activated ion channels in health and disease. *Nat. Rev. Mol. Cell Biol.* **18**, 771–783 (2017).
4. Xiao, B. Levering mechanically activated piezo channels for potential pharmacological intervention. *Annu Rev. Pharm. Toxicol.* **60**, 195–218 (2020).
5. Syeda, R. et al. Chemical activation of the mechanotransduction channel Piezo1. *Elife* **4**, e07369 (2015).
6. Wang, Y. et al. A lever-like transduction pathway for long-distance chemical- and mechano-gating of the mechanosensitive Piezo1 channel. *Nat. Commun.* **9**, 1300 (2018).
7. Evans, E. L. et al. Yoda1 analogue (Dooku1) which antagonizes Yoda1-evoked activation of Piezo1 and aortic relaxation. *Br. J. Pharm.* **175**, 1744–1759 (2018).
8. Del Rosario, J., Gabrielle, M., Yudin, Y. & Rohacs, T. TMEM120A/TACAN inhibits mechanically activated PIEZO2 channels. *J. Gen. Physiol.* **154**, e202213164 (2022).
9. Beaulieu-Laroche, L. et al. TACAN is an ion channel involved in sensing mechanical pain. *Cell* **180**, 956–967 e917 (2020).
10. Niu, Y. et al. Analysis of the mechanosensor channel functionality of TACAN. *Elife* **10**, e71188 (2021).
11. Parpaite, T. et al. Patch-seq of mouse DRG neurons reveals candidate genes for specific mechanosensory functions. *Cell Rep.* **37**, 109914 (2021).
12. Rong, Y. et al. TMEM120A contains a specific coenzyme A-binding site and might not mediate poking- or stretch-induced channel activities in cells. *Elife* **10**, e71474 (2021).
13. Xue, J. et al. TMEM120 is a coenzyme A-binding membrane protein with structural similarities to ELOVL fatty acid elongase. *Elife* **10**, e71220 (2021).
14. Nie, L. et al. The structural basis of fatty acid elongation by the ELOVL elongases. *Nat. Struct. Mol. Biol.* **28**, 512–520 (2021).
15. Naganuma, T., Sato, Y., Sassa, T., Ohno, Y. & Kihara, A. Biochemical characterization of the very long-chain fatty acid elongase ELOVL7. *FEBS Lett.* **585**, 3337–3341, (2011).
16. Gabrielle, M. & Rohacs, T. TMEM120A/TACAN: A putative regulator of ion channels, mechanosensation, and lipid metabolism. *Channels.* **17**, 2237306, (2023).
17. Moroni, M., Servin-Vences, M. R., Fleischer, R., Sanchez-Carranza, O. & Lewin, G. R. Voltage gating of mechanosensitive PIEZO channels. *Nat. Commun.* **9**, 1096 (2018).
18. Romero, L. O. et al. A dietary fatty acid counteracts neuronal mechanical sensitization. *Nat. Commun.* **11**, 2997 (2020).
19. Zhang, P. et al. Lipin 2/3 phosphatidic acid phosphatases maintain phospholipid homeostasis to regulate chylomicron synthesis. *J. Clin. Invest* **129**, 281–295 (2019).
20. Ojeda-Alonso, J. et al. Lack of evidence for participation of TMEM150C in sensory mechanotransduction. *J. Gen. Physiol.* **154**, e202213098 (2022).
21. Verkest, C. et al. Intrinsically disordered intracellular domains control key features of the mechanically-gated ion channel PIEZO2. *Nat. Commun.* **13**, 1365 (2022).
22. Ke, M. et al. Cryo-EM structures of human TMEM120A and TMEM120B. *Cell Discov.* **7**, 77 (2021).
23. Wang, L. & Liu, X. TMEM120A-mediated regulation of chemotherapy sensitivity in colorectal cancer cells. *Cancer Chemother. Pharm.* **93**, 11–22 (2024).
24. Tucker, S. J. & Baukrowitz, T. How highly charged anionic lipids bind and regulate ion channels. *J. Gen. Physiol.* **131**, 431–438, (2008).
25. Lee, B. H., De Jesus Perez, J. J., Moiseenkova-Bell, V. & Rohacs, T. Structural basis of the activation of TRPV5 channels by long-chain acyl-Coenzyme-A. *Nat. Commun.* **14**, 5883 (2023).
26. Uchiyama, A. et al. Inhibition of transcellular tumor cell migration and metastasis by novel carba-derivatives of cyclic phosphatidic acid. *Biochim Biophys. Acta* **1771**, 103–112, (2007).
27. Kakiuchi, Y. et al. Antinociceptive effect of cyclic phosphatidic acid and its derivative on animal models of acute and chronic pain. *Mol. Pain.* **7**, 33 (2011).
28. McDermott, M. I., Wang, Y., Wakelam, M. J. O. & Bankaitis, V. A. Mammalian phospholipase D: function, and therapeutics. *Prog. Lipid Res.* **78**, 101018 (2020).
29. Tei, R. & Baskin, J. M. Spatiotemporal control of phosphatidic acid signaling with optogenetic, engineered phospholipase Ds. *J. Cell Biol.* **219**, e201907013 (2020).
30. Bowling, F. Z., Frohman, M. A. & Airola, M. V. Structure and regulation of human phospholipase D. *Adv. Biol. Regul.* **79**, 100783 (2021).
31. Romero, L. O. et al. Linoleic acid improves PIEZO2 dysfunction in a mouse model of Angelman Syndrome. *Nat. Commun.* **14**, 1167 (2023).
32. Jiang, Y., Yang, X., Jiang, J. & Xiao, B. Structural designs and mechanogating mechanisms of the mechanosensitive piezo channels. *Trends Biochem. Sci.* **46**, 472–488 (2021).
33. Romero, L. O. et al. Dietary fatty acids fine-tune Piezo1 mechanical response. *Nat. Commun.* **10**, 1200 (2019).
34. Ma, S. et al. Excessive mechanotransduction in sensory neurons causes joint contractures. *Science* **379**, 201–206 (2023).
35. Shi, J. et al. Sphingomyelinase disables inactivation in endogenous PIEZO1 channels. *Cell Rep.* **33**, 108225 (2020).
36. Buyan, A. et al. Piezo1 forms specific, functionally important interactions with phosphoinositides and cholesterol. *Biophys. J.* **119**, 1683–1697 (2020).
37. Lin, Y., Buyan, A. & Corry, B. Characterizing the lipid fingerprint of the mechanosensitive channel Piezo2. *J. Gen. Physiol.* **154**, e202113064 (2022).
38. Lin, Y., Buyan, A. & Corry, B. Computational studies of Piezo1 yield insights into key lipid-protein interactions, channel activation, and agonist binding. *Biophys. Rev.* **14**, 209–219 (2022).
39. Chong, J. et al. Modeling of full-length Piezo1 suggests importance of the proximal N-terminus for dome structure. *Biophys. J.* **120**, 1343–1356 (2021).
40. Jiang, W. et al. Crowding-induced opening of the mechanosensitive Piezo1 channel in silico. *Commun. Biol.* **4**, 84 (2021).
41. Borbiro, I., Badheka, D. & Rohacs, T. Activation of TRPV1 channels inhibit mechanosensitive Piezo channel activity by depleting membrane phosphoinositides. *Sci. Signal.* **8**, ra15 (2015).
42. Narayanan, P. et al. Myotubularin related protein-2 and its phospholipid substrate PIP2 control Piezo2-mediated mechanotransduction in peripheral sensory neurons. *Elife* **7**, 7:e32346 (2018).
43. Harayama, T. & Riezman, H. Understanding the diversity of membrane lipid composition. *Nat. Rev. Mol. Cell Biol.* **19**, 281–296 (2018).
44. Chen, X. et al. Cryo-EM structure of the human TACAN in a closed state. *Cell Rep.* **38**, 110445 (2022).
45. Batrakou, D. G., de Las Heras, J. I., Czapiewski, R., Mouras, R. & Schirmer, E. C. TMEM120A and B: nuclear envelope transmembrane proteins important for adipocyte differentiation. *PLoS ONE* **10**, e0127712 (2015).
46. Czapiewski, R. et al. Genomic loci mispositioning in Tmem120a knockout mice yields latent lipodystrophy. *Nat. Commun.* **13**, 321 (2022).
47. Kolesnikov, Y. et al. Phosphatidic acid in plant hormonal signaling: from target proteins to membrane conformations. *Int. J. Mol. Sci.* **23**, 3227 (2022).

48. Raben, D. M. & Barber, C. N. Phosphatidic acid and neuro-transmission. *Adv. Biol. Regul.* **63**, 15–21 (2017).

49. daCosta, C. J., Wagg, I. D., McKay, M. E. & Baenziger, J. E. Phosphatidic acid and phosphatidylserine have distinct structural and functional interactions with the nicotinic acetylcholine receptor. *J. Biol. Chem.* **279**, 14967–14974 (2004).

50. Comoglio, Y. et al. Phospholipase D2 specifically regulates TREK potassium channels via direct interaction and local production of phosphatidic acid. *Proc. Natl Acad. Sci. USA* **111**, 13547–13552, (2014).

51. Yaginuma, S., Omi, J., Kano, K. & Aoki, J. Lysophospholipids and their producing enzymes: their pathological roles and potential as pathological biomarkers. *Pharm. Ther.* **246**, 108415 (2023).

52. Sheng, X., Yung, Y. C., Chen, A. & Chun, J. Lysophosphatidic acid signalling in development. *Development* **142**, 1390–1395, (2015).

53. Nieto-Posadas, A. et al. Lysophosphatidic acid directly activates TRPV1 through a C-terminal binding site. *Nat. Chem. Biol.* **8**, 78–85 (2012).

54. Kittaka, H., Uchida, K., Fukuta, N. & Tominaga, M. Lysophosphatidic acid-induced itch is mediated by signalling of LPA(5) receptor, phospholipase D and TRPA1/TRPV1. *J. Physiol.* **595**, 2681–2698 (2017).

55. Goswami, S. C. et al. Molecular signatures of mouse TRPV1-lineage neurons revealed by RNA-Seq transcriptome analysis. *J. Pain.* **15**, 1338–1359 (2014).

56. Thakur, M. et al. Defining the nociceptor transcriptome. *Front Mol. Neurosci.* **7**, 87 (2014).

57. Usoskin, D. et al. Unbiased classification of sensory neuron types by large-scale single-cell RNA sequencing. *Nat. Neurosci.* **18**, 145–153 (2015).

58. Ranade, S. S. et al. Piezo2 is the major transducer of mechanical forces for touch sensation in mice. *Nature* **516**, 121–125 (2014).

59. Tsugawa, H. et al. MS-DIAL: data-independent MS/MS deconvolution for comprehensive metabolome analysis. *Nat. Methods* **12**, 523–526 (2015).

60. Tsugawa, H. et al. A lipidome atlas in MS-DIAL 4. *Nat. Biotechnol.* **38**, 1159–1163 (2020).

61. Del Rosario, J. S. et al. Gi-coupled receptor activation potentiates Piezo2 currents via Gbetagamma. *EMBO Rep.* **21**, e49124 (2020).

62. Chaplan, S. R., Bach, F. W., Pogrel, J. W., Chung, J. M. & Yaksh, T. L. Quantitative assessment of tactile allodynia in the rat paw. *J. Neurosci. Methods* **53**, 55–63 (1994).

63. Christensen, S. L. et al. Von Frey testing revisited: provision of an online algorithm for improved accuracy of 50% thresholds. *Eur. J. Pain.* **24**, 783–790 (2020).

64. Su, S., Yudin, Y., Kim, N., Tao, Y. X. & Rohacs, T. TRPM3 channels play roles in heat hypersensitivity and spontaneous pain after nerve injury. *J. Neurosci.* **41**, 2457–2474 (2021).

Author contributions
M.G. and T.R. conceptualize the study. M.G. performed all electrophysiology and TIRF experiments and the LC-MS/MS sample preparation. Y.Y. performed the behavioral experiments. Y.W. performed and X.S. supervised the LC-MS/MS experiments. M.G. visualized the data. T.R. supervised the study. T.R. and M.G. wrote the manuscript, all authors reviewed and revised the manuscript.

Competing interests
The authors declare no competing interests.

Additional information
Supplementary information The online version contains supplementary material available at https://doi.org/10.1038/s41467-024-51181-4.

Correspondence and requests for materials should be addressed to Tibor Rohacs.

Peer review information *Nature Communications* thanks Ben Corry, Di Wu, and the other, anonymous, reviewer(s) for their contribution to the peer review of this work. A peer review file is available.

Reprints and permissions information is available at http://www.nature.com/reprints

Publisher's note Springer Nature remains neutral with regard to jurisdictional claims in published maps and institutional affiliations.